

Binaries of massive black holes in rotating clusters: Dynamics, gravitational waves, detection and the role of eccentricity

P. Amaro-Seoane^{1,2*}, C. Eichhorn^{3†}, Edward K. Porter^{4‡}, R. Spurzem^{5,6,7§}

¹Max-Planck Institut für Gravitationsphysik (Albert Einstein-Institut), Am Mühlenberg 1, D-14476 Potsdam, Germany

²Institut de Ciències de l’Espai, IEEC/CSIC, Campus UAB, Torre C-5, parells, 2^{na} planta, ES-08193, Bellaterra, Barcelona, Spain

³Institut für Raumfahrtssysteme, Universität Stuttgart, Pfaffenwaldring 31, 70550 Stuttgart, Germany

⁴Laboratoire APC, UMR 7164, Université Paris 7 Denis Diderot, 10, rue Alice Domon et Léonie Duquet 75205 Paris Cedex 13, France

⁵National Astronomical Observatories of China, Chinese Academy of Sciences, 20A Datun Lu, Chaoyang District, 100012, Beijing, China

⁶Kavli Institute for Astronomy and Astrophysics, Peking University, China

⁷Astronomisches Rechen-Institut, Mönchhofstraße 12-14, 69120, Zentrum für Astronomie, Universität Heidelberg, Germany

10 November 2021

ABSTRACT

The dynamical evolution of binaries of intermediate-mass black holes (IMBHs, massive black holes with a mass ranging between 10^2 and $10^4 M_\odot$) in stellar clusters has recently received an increasing amount of attention. This is at least partially due to the fact that if the binary is hard enough to evolve to the phase at which it will start emitting gravitational waves (GWs) efficiently, there is a good probability that it will be detectable by future space-borne detectors like LISA. We study this evolution in the presence of rotation in the cluster by carrying out a series of simulations of an equal-mass binary of IMBHs embedded in a stellar distribution with different rotational parameters. The survey indicates that eccentricities and inclinations are primarily determined by the initial conditions of the IMBHs and the influence of dynamical friction, even though they are finally perturbed by the scattering of field stars. In particular, the eccentricity is strongly connected to the initial IMBHs velocities, and values of ~ 0.7 up to 0.9 are reached for low initial velocities, while almost circular orbits result if the initial velocities are increased. Evidence suggests a dependency of the eccentricity on the rotation parameter. We found only weak changes in the inclination, with slight variations of the orientation of the angular momentum vector of the binary. Counter-rotation simulations yield remarkably different results in eccentricity. A Monte Carlo study indicates that these sources will be detectable by a detector such as LISA with median signal to noise ratios of between 10 and 20 over a three year period, although some events had signal to noise ratios of 300 or greater. Furthermore, one should also be able to estimate the chirp-mass with median fractional errors of 10^{-4} , reduced mass on the order of 10^{-3} and luminosity distance on the order of 10^{-1} . Finally, these sources will have a median angular resolution in the LISA detector of about 3 square degrees, putting events firmly in the field of view of future electromagnetic detectors such as LSST.

Key words: stellar dynamics – black hole physics – gravitational waves – detection – globular clusters: general

1 INTRODUCTION

Even though their existence are not as well-established as the existence of stellar-mass or supermassive black holes (SMBHs), it is plausible that intermediate-mass black holes (IMBHs; masses $M \sim 10^{2-4} M_\odot$) exist in the centre of stellar clusters (see Miller & Colbert 2004, and references

* E-mail: Pau.Amaro-Seoane@aei.mpg.de

† E-mail: Eichhorn@irs.uni-stuttgart.de

‡ E-mail: porter@apc.univ-paris7.fr

§ E-mail: Spurzem@ari.uni-heidelberg.de

therein). The coalescence of a binary of two massive black holes in that mass range is a powerful source of gravity waves which will be detectable by space-born observatories such as the Laser Interferometer Space Antenna (LISA¹) (Amaro-Seoane & Freitag 2006; Amaro-Seoane et al. 2009).

There are two possible ways to theoretically explain the presence of a binary of IMBHs in a globular cluster. (1) The “single cluster channel”: Gürkan et al. (2006) address this possibility in the scenario of a runaway growth of two stars in a young cluster via physical collisions in the innermost part of the stellar system, where the heaviest stars have sunk through mass segregation (Portegies Zwart & McMillan 2000; Gürkan et al. 2004; Portegies Zwart et al. 2004; Freitag et al. 2006). By adding a fraction of primordial binaries to the cluster, Gürkan et al. (2006) found not one but two independent very massive stars growing in the centre. Eventually, and due to post-Newtonian instabilities, they could collapse and form a massive black hole in the relevant mass range. Amaro-Seoane et al. (2009) followed the evolution of such a binary with direct-summation N -body simulations and estimated that, in some cases, one can expect a residual eccentricity as high as 0.3 for the binary when it enters the LISA band. (2) The “double cluster channel”: Amaro-Seoane & Freitag (2006) discussed an alternative way to form binaries of IMBHs in stellar clusters. It has been observed that in star forming regions such as the Antennæ or Stephan’s Quintet, hundreds of young massive star clusters are clustered into larger complexes of a few 100 pc across (Whitmore et al. 1999; Zhang & Fall 1999; Gallagher et al. 2001). These clusters contain typically some $\sim 10^5$ stars within a few parsecs and it is most likely that some of them are bound (Dieball et al. 2002). Also, most of the clusters in binaries are coeval and younger than 300 Myr, which means that they merge early. Amaro-Seoane & Freitag (2006) followed the evolution of two IMBHs initially located at the centre of two such clusters which collide, and studied the orbital decay to the centre.

The evolution of the orbital parameters of the binary of massive BHs is determined by the stellar dynamics and the emission of GWs, which is negligible at long distances but becomes more and more dominant as the semi-major axis of the binary shrinks. In order to understand the distribution of parameters we can expect for these systems when they enter the window of detection of LISA, it is important to analyse the dynamical story of the binary in detail. The evolution starting at distances at which dynamical friction is important down to the phase of strong emission of GWs – and their detection and characterisation – is a complex and long process which requires different techniques to address it.

One can distinguish roughly three different regimes in the process: (i) at the beginning, the massive BHs are at distances in which GWs, though always present, are totally negligible and the evolution is dominated purely by the dynamics. At this stage, dynamical friction will sink the two massive BHs down to the centre. The perturbers, the single massive BHs in our case, are moving through a sea of small stars (as compared to their masses). The velocity vec-

tor of the stars are rotated after deflecting with the IMBHs. The projected component in the direction of the deflection is shorter. Hence, the massive object, the IMBH, is cumulating just after it a high-density stellar region. The perturber will feel a drag from that region from the conservation of J in the direction of its velocity vector. The direction does not change to first-order, but the amplitude decreases. A drag force starts to act on the perturber, so that it slows down as it sinks down to the centre of the stellar system. This force happens to be proportional the square of the mass of the perturber so, the bigger the mass of the perturber, the bigger the dynamical effects, in spite of the bigger inertia. (ii) As they approach closer and closer, the two massive BHs form a bound state, a binary system. At this stage, the binary interacts strongly with stars coming from the surrounding stellar system. Since the stars have a much smaller mass, the outcome of the interaction is that a star is slingshot into the stellar system with a higher kinetic energy, gained from the removal of energy and angular momentum of the binary; therefore, the semi-major axis of the binary, a , shrinks a bit more. These interactions mostly tend to increase the eccentricity of the binary (iii) The process is repeated again and again, provided the reservoir of stars is not empty – in which case the loss-cone would be depleted –, until the separation between the members of the binary is small enough that the emission of GWs is strong enough as to take over the dynamics as the main factor of evolution of the orbital parameters. The binary is practically isolated from the stellar system. Thereafter, the binary begins to circularise. Obviously, the transition between these phases in the evolution is not well-separated and the whole evolution requires numerical tools to investigate it. Amaro-Seoane & Freitag (2006); Amaro-Seoane et al. (2009) addressed some of these questions in the context of globular clusters and IMBHs. They proved, with N -body models, that slingshot ejections of stars increase the eccentricity of the IMBH binary to ~ 0.8 and beyond and that later the emission of GWs then circularises the orbit to rather low, yet detectable values of eccentricity.

But Nature is more complex than that. A key effect that will determine the global evolution of both the cluster and of the massive binary of IMBHs is the rotation of the stellar system. Rotation has been identified in clusters for a long time. Deviations from spherical symmetry were discovered in some globular clusters (Shapley 1930) as early as the beginning of the last century. This flattening is a fingerprint for rotation and the measurements of ellipticity were later extended to galactic and extragalactic globular clusters (see e.g. White & Shawl 1987; Staneva et al. 1996). One can also detect rotation by measuring radial velocities of individual stars in the globular clusters (Meylan & Mayor 1986; Gebhardt et al. 2000; Reijns et al. 2006).

Amaro-Seoane & Freitag (2006) first addressed this problem focusing on the detection of GWs in the context of a binary of IMBH formed as the result of a collision of two clusters; Amaro-Seoane et al. (2009) looked at the same problem from the perspective of a born-in binary, extended the study to multi-mass clusters and non-equal mass binaries and described the global dynamical evolution with the implication of the larger eccentricities they found in a general context of detection.

¹ <http://lisa.nasa.gov/>, <http://sci.esa.int/science-e/www/area/index.html> and <http://www.esa.int/ESA/Science/Projects/LISA> The eccentricity of the binary is decisive

in the study. Direct summation N -body models, including post-Newtonian corrections, show that the stellar dynamical history before the relativistic regime can significantly affect the final evolution and leads to different merger times (Berentzen et al. 2009). In particular, it turns out that massive binaries may enter the relativistic phase with high eccentricities, and signatures of the eccentricities are kept in the harmonics of the gravitational waveforms until the moment of coalescence (Amaro-Seoane & Freitag 2006; Amaro-Seoane et al. 2009; Berentzen et al. 2009). The evolution of the eccentricity has been previously discussed in a number of articles (Makino et al 1993; Hemsendorf 2000; Milosavljević & Merritt 2001; Hemsendorf et al 2002; Berczik et al. 2005; Amaro-Seoane & Freitag 2006; Berczik et al 2006; Amaro-Seoane et al. 2009; Berentzen et al. 2009).

As derived by Peters (1964), the orbit-averaged timescale of coalescence due to the emission of gravitational radiation is given by

$$t_{\text{GW}} = \frac{5}{64} \frac{c^5 a_{\text{GW}}^4}{G^3 M_1 M_2 (M_1 + M_2) F(e)} \quad (1)$$

where M_1, M_2 denote the black hole masses, a_{GW} the characteristic separation for gravitational wave emission, G the gravitational constant, c the speed of light and

$$F(e) = (1 - e^2)^{-7/2} \left(1 + \frac{73}{24} e^2 + \frac{37}{96} e^4 \right) \quad (2)$$

is a function with dependence on the eccentricity e . Thus the coalescence time can shrink by several orders of magnitude if the eccentricity is high enough, resulting in a stronger burst of gravitational radiation and different characteristic waveforms. Furthermore, the behavior of the the inclination of the orbital plane is potentially interesting in predicting processes related to angular momentum exchange between IMBHs and field stars.

A natural continuation of the analysis carried out until now is to add another physical factor to the problem, the rotation of the system, since it can have a very important impact in the global dynamics of the cluster. It can also particularly effect the evolution of the eccentricity of the binary and, thus, the detection and characterisation of the GW observation.

From a standpoint of the data analysis of such GWs for LISA, because of their low mass –as compared to SMBH binaries–, IMBH binaries should be visible at moderate to high frequencies in the LISA detector. As most of these binaries coalesce outside the LISA band, they will be observable in the detector throughout the lifetime of the mission. This should allow us to confidently detect and estimate the parameters for such systems. If such sources exist in the LISA data stream, it will also allow us, assuming a strong enough signal, to provide accurate distance measurements in the local universe.

The structure of this paper is as follows: We start by giving a description of the numerical method used for the simulations in section (2); later, in section (3) we give a short overview of the initial conditions we use for the numerical study; in section (4) we provide a detailed analysis of the dynamics of the system, i.e. evolution of the binding energy, ec-

centricity and inclination of the IMBH binary; in section (5) we study some cases in which the binary is initially set up on a counter-rotating orbit in relation to the stellar system in which it is embedded and study the associated Brownian motion; in section (7) we discuss about the implications for lower-frequency Astrophysics and the detectability of such systems. In the last section (8) we summarise the results and give the conclusions of the study.

2 NUMERICAL METHOD

The simulations in this work have been performed using NBODY6++, a parallelised version of Aarseth's NBODY6 (Spurzem 1999). The code includes a Hermite integration scheme, KS-regularisation (Kustaanheimo & Stiefel 1965) and the Ahmad-Cohen neighbour scheme (Ahmad & Cohen 1973). No softening has been introduced; this circumstance allows an accurate treatment of the effects due to super-elastic scattering events, which play a crucial part in black hole binary evolution and require a precise calculation of the trajectories throughout the interaction.

Additionally, in order to improve the exactness of computation of the motion of particles in the environment of the black holes, a modification in the determination of the neighbour radius in the Ahmad-Cohen scheme was implemented. In principle, the Ahmad-Cohen scheme divides the force on a particle into a regular and an irregular component, assigning both forces different time steps; the irregular component is computed over the nearest particles populating an area called the neighbour sphere. Normally, the neighbour sphere, which is in its extension defined by the neighbour radius, is characterised as containing a defined number of stars n_n , which is typically set to $n_n = 50$ in simulations dealing with particle numbers of the order presented here. However, when considering a scenario consisting of two heavy particles of the same mass, embedded in a stellar component of equal-mass particles, the neighbour radius is enlarged by a factor

$$\gamma = \beta \left[\left(\frac{1}{2} \left(\frac{m_i}{m_j} + \frac{m_j}{m_i} \right) \right)^\lambda - 1 \right] + 1 \quad (3)$$

if during the declaration of the neighbour particles of a particle j and the neighbour candidates i a mass difference $m_i/m_j \neq 1$ occurs (Hemsendorf 2000). The enlargement factor γ is symmetric in the masses m_i and m_j . As a result, massive particles (black holes) receive a larger neighbour radius, and a massive particle is also more likely declared as neighbour of a stellar particle. This method accommodates the influence of a black hole on its surroundings and lessens the underestimation on that stellar component which possessed a black hole nearby, but outside the neighbour sphere in the scheme without the enlargement factor. The parameters β and λ have been set $\beta = 0.03$ and $\lambda = 1$, yielding $\gamma = 10.57$, consistent with the simulations presented by Hemsendorf et al (2002).

Set	Model	W_0	ω_0	v_0	r_c	v_c	$T_{\text{rot}}/T_{\text{kin}}$
1	\mathcal{A}	3	0.0	$\sqrt{2}v_c$	0.396	0.552	0
	\mathcal{B}	3	0.0	v_c	0.396	0.552	0
	\mathcal{C}	3	0.0	$0.136v_c$	0.396	0.552	0
2	\mathcal{D}	3	0.3	$\sqrt{2}v_c$	0.400	0.558	0.01
	\mathcal{E}	3	0.3	v_c	0.400	0.558	0.01
	\mathcal{F}	3	0.3	$0.136v_c$	0.400	0.558	0.01
3	\mathcal{G}	3	0.6	$\sqrt{2}v_c$	0.415	0.555	0.0343
	\mathcal{H}	3	0.6	v_c	0.415	0.555	0.0343
	\mathcal{I}	3	0.6	$0.136v_c$	0.415	0.555	0.0343
4	\mathcal{J}	6	0.0	$\sqrt{2}v_c$	0.239	0.563	0
	\mathcal{K}	6	0.0	v_c	0.239	0.563	0
	\mathcal{L}	6	0.0	$0.136v_c$	0.239	0.563	0
5	\mathcal{M}	6	0.3	$\sqrt{2}v_c$	0.256	0.553	7
	\mathcal{N}	6	0.3	v_c	0.256	0.553	7
	\mathcal{O}	6	0.3	$0.136v_c$	0.256	0.553	7
6	\mathcal{P}	6	0.6	v_c	0.320	0.550	19.81
	\mathcal{Q}	6	0.6	$0.136v_c$	0.320	0.550	19.81

Table 1. Overview over the initial conditions of all simulations. All values are expressed in N-body units. W_0 is the King parameter, ω_0 the rotation parameter, v_0 the initial velocity of the IMBHs, r_c the core radius, v_c the central velocity and $T_{\text{rot}}/T_{\text{kin}}$ is the ratio of rotational energy and total kinetic energy at time $T = 0$. We use $\gamma = \gamma_3$, $\beta = 0.03$, $\lambda = 1.0$. In all simulations $\eta_{\text{reg}} = 0.02$, whilst $\eta_{\text{irreg}} = 0.02$ for the cases $\mathcal{A} - \mathcal{I}$ and 0.01 for the cases $\mathcal{J} - \mathcal{Q}$.

3 INITIAL CONDITIONS

In all our simulations, the conversion factors are as follows: A unit of length is equivalent to $U_{\text{L}}^{\text{NB}} = 1.1$ pc, a unit of mass to $U_{\text{M}}^{\text{NB}} = 43921.6M_{\odot}$, a unit of velocity to $U_{\text{V}}^{\text{NB}} = 13.233$ km/s and a unit of time to $U_{\text{T}}^{\text{NB}} = 8.14 \cdot 10^{-2}$ Myrs. The set of simulations was carried out for a total particle number $N = 64000$, including two massive black holes $M_1 = M_2 = 0.01$ embedded in a dense stellar system of 63998 equal-mass particles $m_* = 1.5625 \cdot 10^{-5} U_{\text{M}}^{\text{NB}}$. The initial stellar distribution satisfies a rotating King model,

$$f(E, L_z) = \begin{cases} \text{const} \times \left(e^{-\beta(E - \Phi_t)} - 1 \right) e^{\beta\Omega_c L_z} & E < \Phi_t \\ 0 & E \geq \Phi_t \end{cases} \quad (4)$$

where $\beta = 1/\sigma^2$ represents the inverse one-dimensional velocity dispersion, E and L_z the energy and the z-component of the angular momentum of a star per unit mass, and Φ_t the tidal potential of the model. The King parameters W_0 and ω_0 are defined by $W_0 = -\beta(\Phi_0 - \Phi_t)$ and $\omega_0 = \sqrt{9/4\pi G\rho_c} \cdot \Omega_c$ with the parameters Φ_0 representing the central potential, ρ_c a mass density and Ω_c approximately the angular velocity in the centre (Einsel & Spurzem 1999; Lagoute & Longaretti 1996; Longaretti & Lagoute 1996).

A symmetric set-up underlies all simulations, with the rotation axis of the King model in the z-direction and the two black holes located in the xy-plane on the opposite side of the cluster on the core radius r_c of the model. Thereby, the usual definition of the core radius in N-body simulations,

$$r_c = \left(\frac{\sum_{j=1}^{N^*} \rho_j^2 |\mathbf{r}_j - \mathbf{r}_d|^2}{\sum_{j=1}^{N^*} \rho_j^2} \right)^{1/2} \quad N^* \geq N/5, \quad (5)$$

is used (Aarseth 2003), where $\mathbf{r}_d = \sum_{j=1}^N \rho_j \mathbf{r}_j / \sum_{j=1}^N \rho_j$ is the density centre of the system consisting of particles of the mass m with the coordinates \mathbf{r}_j , and $\rho_j = 3(k-1)m/4\pi r_j^{3(k)}$ the local density in an area around each particle j (Casertano & Hut 1985). The quantity $r_j^{(k)}$ is to be interpreted as the radius of the sphere over which the local density is evaluated, characterised in size by the number of stars k populating this volume. Applying this formalism, $k = 6$ is the optimal choice. The summation in equation 5 is restricted to the innermost $N/5$ particles, which saves computation time while showing coevally adequate agreement with an exact calculations. The initial velocities are adjusted in the xy-plane tangential to a circle around the centre, adopting the values $v_0 = 0.136v_c, v_c$ and $\sqrt{2}v_c$ in terms of the circular velocity v_c . Scenarios with the black holes moving initially with, as well as contrary to, the rotation of the stellar system have been investigated.

The evolution of the black hole binary was followed using King parameters $W_0 = 3; 6$ and $\omega_0 = 0.0; 0.3; 0.6$. We have chosen these parameters because they are representative for the problem we want to address in this work, from the absence of rotation to a rather high value. Typical values for ω_0 in globular clusters range between 0.1 and 0.5. For instance, ω_{Cen} has a value of 0.5, N2808 of 0.3, 47Tuc of 0.15, N5286 of 0.5 etc (Fiestas et al 2006).

The accuracy was tuned in such a way that relative energy errors measured over one NBODY time were $< 10^{-3}$ concerning $W_0 = 3$ and $< 10^{-4}$ concerning $W_0 = 6$ simulations respectively. The complete survey of investigations is shown in Tab.1.

4 DYNAMICS OF THE SYSTEM

4.1 Evolution of the binding energy

The total energy of the binary in a two-body approximation is given by

$$E = \frac{\mu}{2} \dot{r}^2 + \frac{l^2}{2\mu r^2} - \frac{GM_1 M_2}{r} \quad (6)$$

where r denotes their separation, M_1 and M_2 the black hole masses, $\mu = M_1 M_2 / (M_1 + M_2)$ the reduced mass, l the angular momentum and G the gravitational constant.

Fig. 1 shows the time evolution of the total energy. In both cases, the initial velocity is $v_0 = 0.136v_c$ on the core radius, different colours represent different rotational parameters. Naturally, as long as the gravitational force of the stellar system dominates the motion of the black holes, the two-body energy is not very meaningful. Initial oscillations are the result of this invalidity: Due to the symmetric set-up both black holes reach the apoapsis and the periapsis almost simultaneously, in the apoapsis (where their separation is at maximum, which consequently means a local minimum in the total energy) the black holes are formally bound to each other ($E < 0$). However, they feel the potential of the stellar system not included in eq.6 and are accelerated to the centre while gathering kinetic energy in such a way that the bound

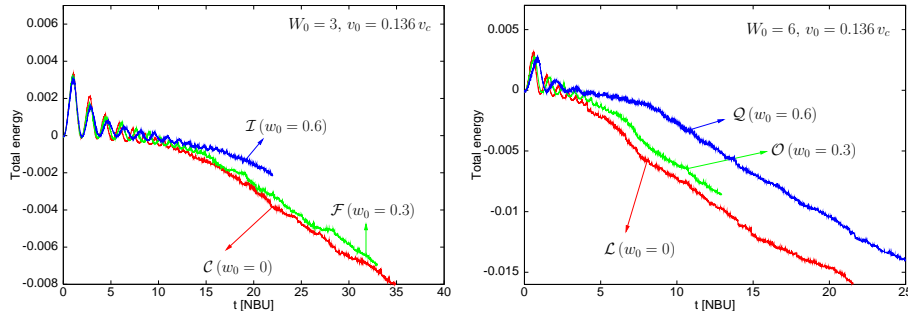


Figure 1. *Left panel:* Evolution of the total energy of the IBMH binary for the models \mathcal{I} , \mathcal{F} and \mathcal{C} (from the top to the bottom at later times; in the on-line version of the paper displayed in blue, green and red respectively) *Right panel:* As in the previous panel, for models \mathcal{Q} , \mathcal{O} and \mathcal{L}

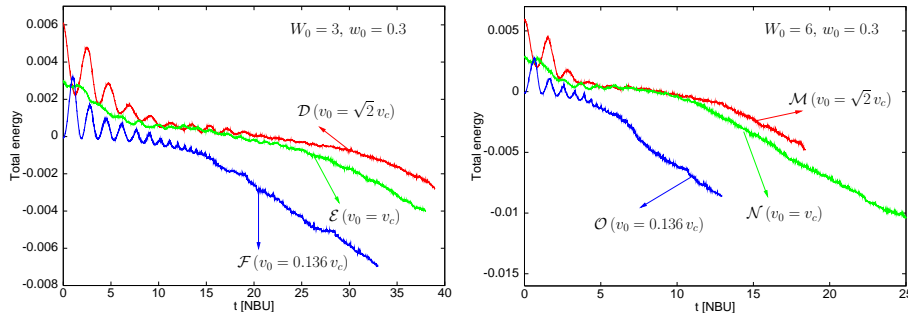


Figure 2. *Left panel:* Same as Fig.(1) for models \mathcal{D} , \mathcal{E} and \mathcal{F} . In this case all models have the same King parameter $W_0 = 3$ and $w_0 = 0.3$, so that they differ only in the initial velocities (from the top to the bottom at later times $v_0 = \sqrt{2}v_c$, $v_0 = v_c$ and $v_0 = 0.136v_c$, depicted in the on-line version in red, green and blue, respectively) *Right panel:* As in the previous panel but with $W_0 = 6$, for models \mathcal{M} , \mathcal{N} and \mathcal{O}

Model	σ_0^2	$\frac{n_0}{10^3}$	$\frac{1}{a_h}$	H
\mathcal{C}	0.526	41.06	210	7.8 ± 2.0
\mathcal{F}	0.522	43.53	209	7.2 ± 1.9
\mathcal{J}	0.478	117.12	191	5.2 ± 1.3
\mathcal{K}	0.478	117.12	191	5.6 ± 1.5
\mathcal{L}	0.478	117.12	191	6.1 ± 1.6
\mathcal{N}	0.468	108.04	187	5.8 ± 1.5
\mathcal{O}	0.468	108.04	187	6.8 ± 1.7
\mathcal{Q}	0.425	64.79	170	10.4 ± 2.7

Table 2. The hardening constants determined in simulations for a variety of models and initial conditions. σ_0 represents the initial central velocity dispersion, n_0 the initial central particle density, a_h the characteristic separation for hardening via super-elastic scattering processes and H the hardening constant.

state is resolved. In this first stage, each black hole individually suffers dynamical friction, which is the main process of losing energy.

The role of dynamical friction decreases when a permanently bound state occurs (the energy remains negative), as the dynamical friction force acts primarily on the motion of the now formed binary rather than on the individual black holes. Super-elastic scattering events of field stars at the binary become more and more important for the reduction of its energy. These events become visible in the tiny-

peak structure that appears in each curve in Fig.1 at times $t \gtrsim 17$ for $W_0 = 3$ and $t \gtrsim 8$ for $W_0 = 6$ respectively. In the stage where super-elastic scattering dominates the picture, the energy loss rate is commonly written in terms of the dimensionless hardening constant H

$$\frac{d}{dt} \left(\frac{1}{a} \right) = HG \frac{\rho}{\sigma} \quad (7)$$

where a is the separation of the black holes, ρ the mass density and σ the velocity dispersion in the environment of the binary (see e.g. Merritt 2001). The constant slope of the energy in Fig.1 is expected from eq.7 with $\rho/\sigma = \text{const.}$

In Tab.2, hardening constants have been determined for scenarios in which a constant energy loss rate had developed before the simulation ended. The time derivative of the inverse separation was taken from the slope of the curves in Fig.1, which is connected to the energy by $E = -GM/2a$. Approximately, $\sigma/\rho = \sigma_0/\rho_0$ was assumed with ρ_0 and σ_0 as initial values within the 1% Lagrangian radius of the model. As this represents a rather vague approximation, a 25% range of this ratio was combined with an regression estimate of the uncertainties in slope designation to obtain the error margins.

Since the stage which is dominated by superelastic scattering is reached sooner if the central potential of the stellar distribution is deeper, the hardening constants have been calculated primarily for runs with $W_0 = 6$ in Table 2. For these runs, the separation of the IMBHs has fallen below the characteristic separation $a_h = GM/4\sigma_0^2$ at the end of

the simulation, which indicates that the system is in the hardening regime.

The values of the hardening constants are in majority slightly below compared to the $H = 8.4$ published by Hemsendorf et al (2002), where a Plummer model was used. The lower values can be possibly explained by the fact that dynamical friction might still have a noticeable influence. Regarding our calculated a_h as criteria for the domination of super-elastic scattering events, the hardening separation could be significantly smaller if σ increases during the simulation as $a_h \propto \sigma^{-2}$. An enhanced σ can be expected for $\rho/\sigma = \text{const.}$ if it is assumed that the black hole would capture stars during the simulation and raise the central density.

We can see in Fig. 1 that King potentials of $W_0 = 3$ as well as $W_0 = 6$ the two-body energy reaches higher values (i.e. the system is less bound) at a given time for $\omega_0 = 0.6$, as compared to the simulations with $\omega_0 = 0.0$ and $\omega_0 = 0.3$. Additionally, we find that in the presence of faster rotation $\omega_0 = 0.6$, the transfer of angular momentum to the field stars is inhibited during the first 2–4 time units. This can lead to the circularising of the IMBHs trajectories and, indeed, we find remarkable smaller eccentricities for this case (see Fig 6 of next section).

Variation of the initial velocities is presented in Fig.2. In simulations with $v_0 = v_c$, no oscillations occur in the first time units, as the black holes spiral to the centre symmetrically on circular-like orbits.

4.2 Eccentricity

The eccentricity is determined by

$$e = \sqrt{1 + \frac{2El^2}{\mu(GM_1M_2)^2}} \quad (8)$$

Fig.3 shows the complete survey over calculated eccentricity evolution. Each plot shows simulations of a fixed pair of King parameters under variation of the initial velocity. In the case of $W_0 = 6$, $\omega_0 = 0.6$, no simulation could be performed with $v_0 = \sqrt{2}v_c$ without overstepping the error limits mentioned in section 3 holding the set of NBODY accuracy parameters. The runs were stopped when a fixed physical calculation time of the PC cluster was exceeded.

Initial oscillations appear for the same reasons as in the plots of the total energy previously discussed. After the binary has been formed, and in principle represents a two body system perturbed by encountering field stars, the eccentricity converges to a fixed value that underlies at most a weak drift. This behaviour is consistent with previous work (Hemsendorf 2000; Hemsendorf et al 2002). When the eccentricity has swung into a certain level, again a tiny-peak structure develops as the result of super-elastic scattering processes of field stars at the hardening binary. Note that following the swing-in-procedure, the stochastic fluctuations are of the same order, due to the logarithmic scaling.

All simulations displayed in Figure 3 with an initial velocity comparable to the circular velocity, tend to end up in low-eccentricity motions of the black hole components, while $v_0 = 0.136v_c$ runs reach generally higher final eccentricities. This behaviour was already indicated by Makino et al (1993), who simulated two black holes of the masses $M = 0.01$ in a Plummer sphere of 16348 particles. They found

very high final eccentricities $e \sim 0.99$ applying very low initial velocities, while their largest value, $v_0 = 0.5v_c$, reached a noticeably smaller final $e \sim 0.665$. Investigations carried out by Hemsendorf (2000) and Hemsendorf et al (2002) used initial velocities $v_0 = 0.136v_c$, their high eccentricities were verified in the simulations presented here for the rotating King model.

The dependency of the final eccentricity on initial velocities can be understood by considering the black hole trajectories. In Fig. 4, for $v_0 = v_c$, the black holes spiral, at first independently of each other, to the centre. The influence of dynamical friction causes a steady loss of kinetic energy. Within the time interval $t = [10.11; 20.14]$, the total energy becomes negative and the binary reaches a bound state; subsequently the binary hardens, the separation decreases due to super-elastic scattering events and the circular motion of the centre of mass of the binary itself becomes visible. At the time the attractive force between the black holes becomes comparable to the gravitational force of the stellar distribution, the individual trajectories of the black holes are still circular around the systems centre of mass. This means that the circular orbits generated by the initial velocity is "conserved" until the binary reaches a bound state and beyond, since dynamical friction is not strong enough to change the trajectories dramatically.

A different situation is obtained for $v_0 = 0.136 v_c$. As a consequence of the low velocity, the black holes must plunge near to the centre, but dynamical friction is, at the time of the closest encounter (the periapsis of the relative motion), not sufficiently effective to prevent the re-swing to the outer regions and to circularise the orbits in this way. Therefore, the initial form of the orbits is kept until the end of the simulation. The initial velocity $v_0 = \sqrt{2}v_c$ is also non-circular. The deviations from the previous case are due to the fact that dynamical friction is stronger at apoapsis.

Tab. 3 summarises the results of the complete study. The mean values of the eccentricity \bar{e} , the error of the single value s_e and the error of the mean value $s_{\bar{e}}$ have been calculated over time intervals in which the eccentricity remains stable, and are based on output data of a step-width of 0.002 N-body units. The quantity e_{trans} represents a mean value of the eccentricity in a period the total energy snaps of into the stage of constant energy loss. Although the the eccentricity still undergoes vigorous fluctuations at that time, this transition mean value e_{trans} does not evidently differ from the \bar{e} . It is remarkable that eccentricity develops in a dynamical friction dominated period. The strength of the dynamical friction force along the trajectory of the black holes is crucial whether the individual motion determined by the initial velocities can be kept until the binary forms.

The existence of drifts in eccentricity was reported in previous papers (see introduction). This behaviour can be connected to the effect of super-elastic scattering events. Although the effect of super-elastic scatterings on the eccentricity during the formation of the binary may be only weak, the long term evolution might increase the eccentricity significantly. However, the question, whether the eccentricity is ultimately increased or decreased, cannot be solved here since the simulations includes both rising and declining drifts, as seen for $W_0 = 6$, $\omega_0 = 0.0$ with $v_0 = v_c$ and $v_0 = \sqrt{2}v_c$ (Fig.3, for example). If superelastic scattering

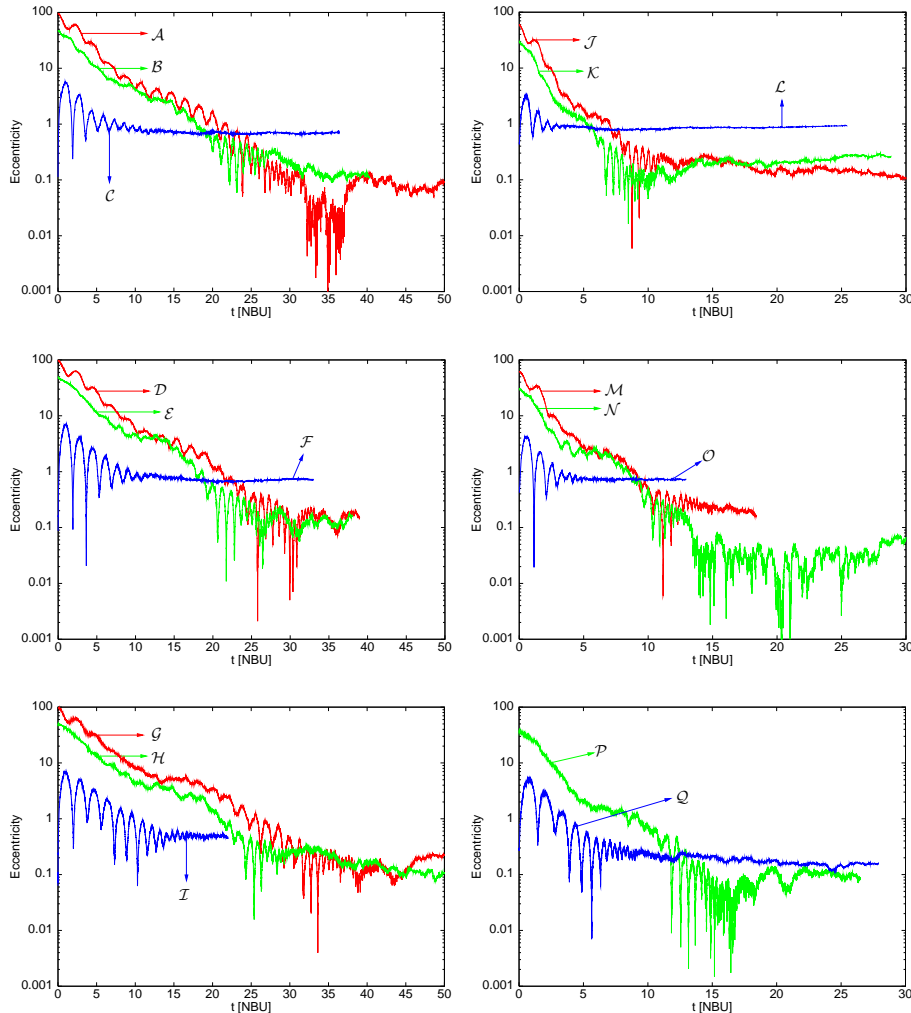


Figure 3. Evolution of the eccentricity of the IMBH binary for the complete survey. Starting from the top and from the left to the right, we display in each panel only three models for readability. In each individual panel, and from the top to the bottom at $t = 0$, we show (in red, green and blue in the on-line version): A, B, C in the first panel, J, K, L in the second one, D, E, F in the third one, M, N, O in the fourth one, G, H, I in the fifth one and P, Q in the last one

should actually increase the eccentricity in long-term evolution, another effect overlays the simulations in that period.

We depict in Fig. 6 the cases F, C, I, O, L and Q of Fig. 3 together in order to illustrate clearly the influence of rotation on the development of eccentricity. With a rotation parameter $\omega_0 = 0.6$, the end value of eccentricity drops significantly for $W_0 = 3$ as well as for $W_0 = 6$. In the case of $W_0 = 3, \omega_0 = 0.6$, no effective transfer of angular momentum to the field stars takes place until $t \sim 5$, with $W_0 = 6, \omega_0 = 0.6$ till $t \sim 2$, thus the trajectories of the IMBHs experience a noticeable truncation in the co-rotating stellar system at the beginning, which finally results in low eccentricities.

4.3 Inclination and angular momentum orientation

The direction of the orbital angular momentum vector of the binary is specified by the quantities

$$\cos i = \mathbf{1} \cdot \hat{\mathbf{e}}_z / l \quad 0 \leq i < \pi \quad (9)$$

and

$$\begin{cases} \cos \Omega = \mathbf{K} \cdot \hat{\mathbf{e}}_x / K & \mathbf{K} \neq 0 \\ \Omega = 0 & \mathbf{K} = 0 \end{cases} \quad 0 \leq \Omega < 2\pi \quad (10)$$

where $\hat{\mathbf{e}}_x$ and $\hat{\mathbf{e}}_z$ are the unit vectors of the reference coordinate system and \mathbf{K} the vector in the direction of the ascending node, $\mathbf{K} = \hat{\mathbf{e}}_z \times \mathbf{l}$, which represents the definition of the inclination i and the longitude of the ascending node Ω following classical celestial mechanics.

The left side of Fig. 7 shows the evolution of the inclination for $W_0 = 6$ and $\omega_0 = 0.6$ for different initial velocities. The inclination, typically in all simulations undergoes comparatively strong changes during the dynamical friction dominated regime, and remains passably stable or slightly drifting during the hardening stage. Nevertheless, the total changes of the inclination angle considering the whole simulation are rather small. Sometimes a monotonic increase of

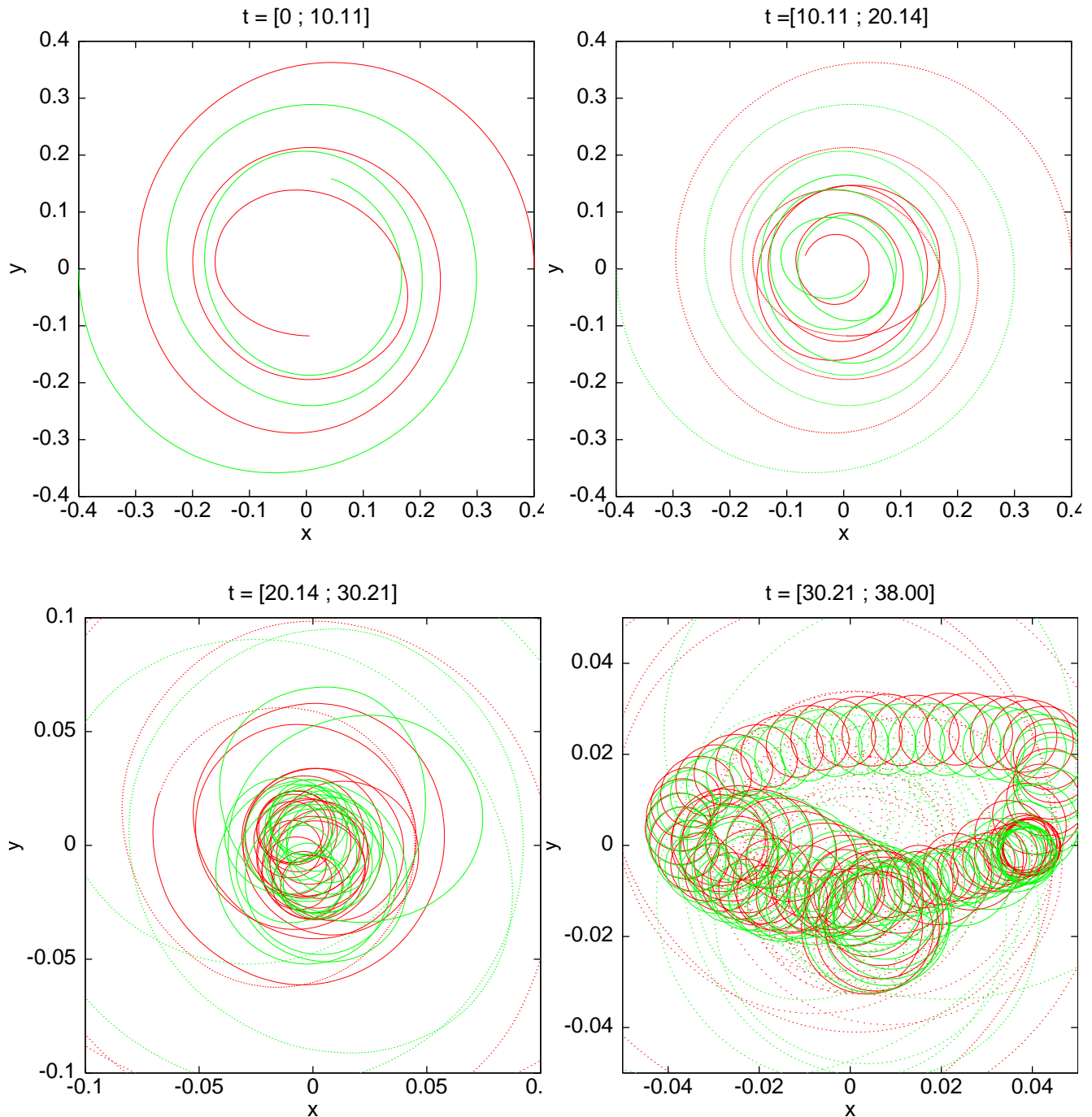


Figure 4. Projection in the X–Y plane of the trajectories of the two IMBHs in the model \mathcal{E} (different colours depict different IMBHs). Solid lines indicate the trajectories passed through in the time interval mentioned above each figure; the dotted lines show the previous orbit. Note the scaling of the axes in different figures; the two lower panels are a zoom in

the inclination angle occurs during the dynamical friction dominated stage, and there were also simulations in which the inclination dropped before reaching stable behaviour. This can be seen in Tab. 4, where the maximum inclination i_{\max} and the mean value seen in the stable phase \bar{i} of each simulation are listed: i_{\max} and \bar{i} can differ considerably.

In the right side of Fig. 7, the direction of the orbital angular momentum vector is illustrated using polar representation ($i \cos \Omega, i \sin \Omega$). The $(0, 0)$ coordinate corresponds

to a rotation of the binary in the xy -reference plane. The extensive ripples are the result of periodic motion before the binary is bound or when the binding is weak. With progressing evolution, the system concentrates in confined cloud-like areas. The measured changes of direction of the orbital angular momentum vector are consistent in order of magnitude with the simulations of Milosavljević & Merritt (2001), with the exception of the inclination maverick $W_0 = 6$, $\omega_0 = 0.0$, $v_0 = 0.136v_c$.

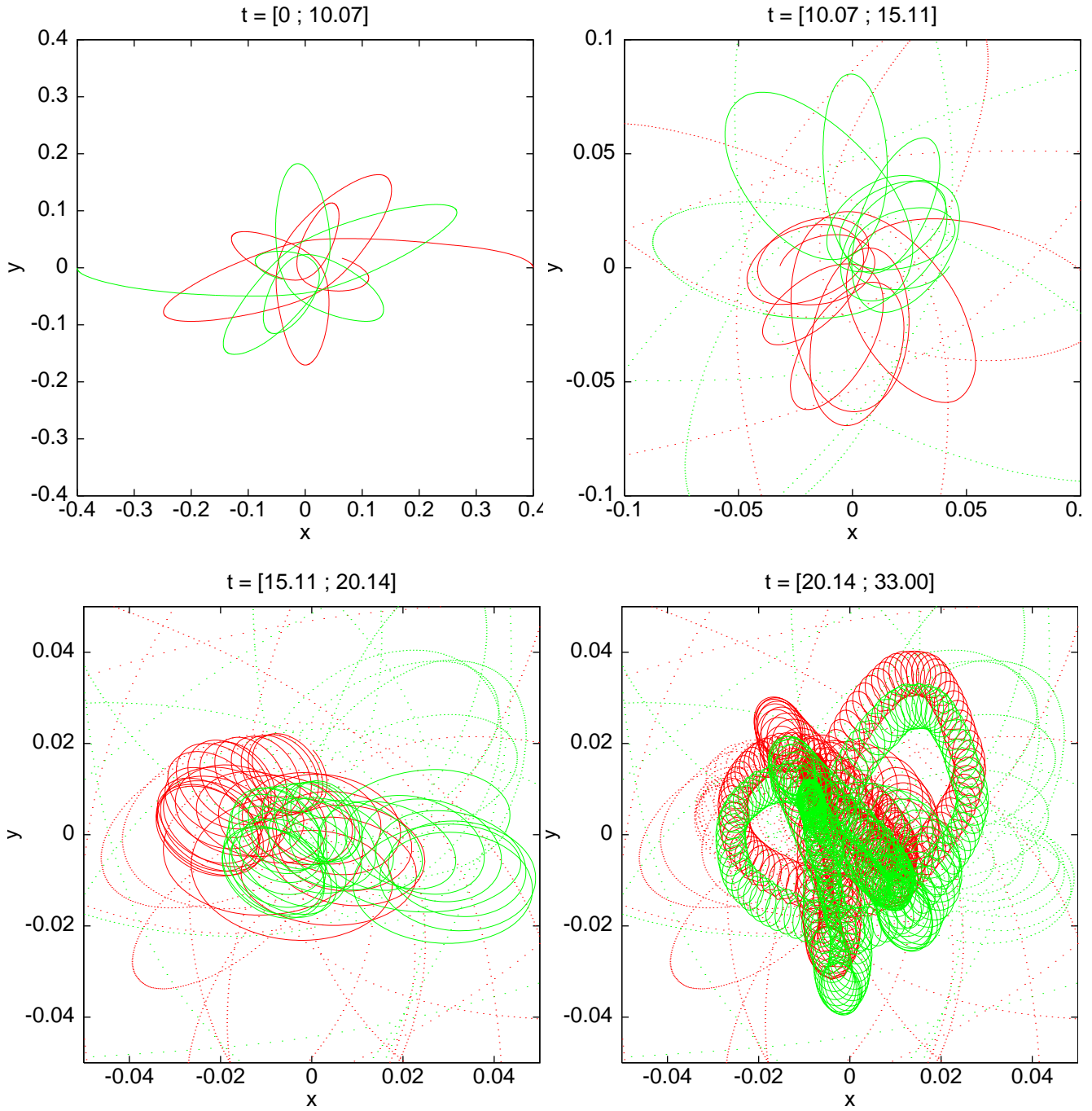


Figure 5. the same as in Fig.4, but for model \mathcal{F}

5 COUNTER ROTATION

Applying exactly the same initial model for the field stars of the corresponding model, the initial velocities of the IMBHs were set contrary the rotation of the stellar system for the models \mathcal{O} and \mathcal{N} .

The distinct influence of dynamical friction during the the first time intervals is responsible for different results in eccentricity evolution compared to the *co*-rotating simulation (Fig. 8). In the case of $v_0 = 0.136v_c$, for *counter*-rotation an extremely high eccentricity $\bar{e} = 0.997$ is reached

($\bar{e} = 0.728$ for *co*-rotating). In this scenario, the relative velocity between a black hole and the field stars is increased at the apoapsis as well as at the periapsis. Dynamical friction is very efficient at the apoapsis of the individual black hole motion in the unbound regime. Thus the black holes suffer a strong energy loss and fall steeper to the centre than in the *co*-rotating simulation. The resulting high eccentric motion is kept into the bound state. Applying an initial velocity $v_0 = v_c$, a higher eccentricity $\bar{e} = 0.160$ occurs compared to the *co*-rotating $\bar{e} = 0.039$, but remains on a low level.

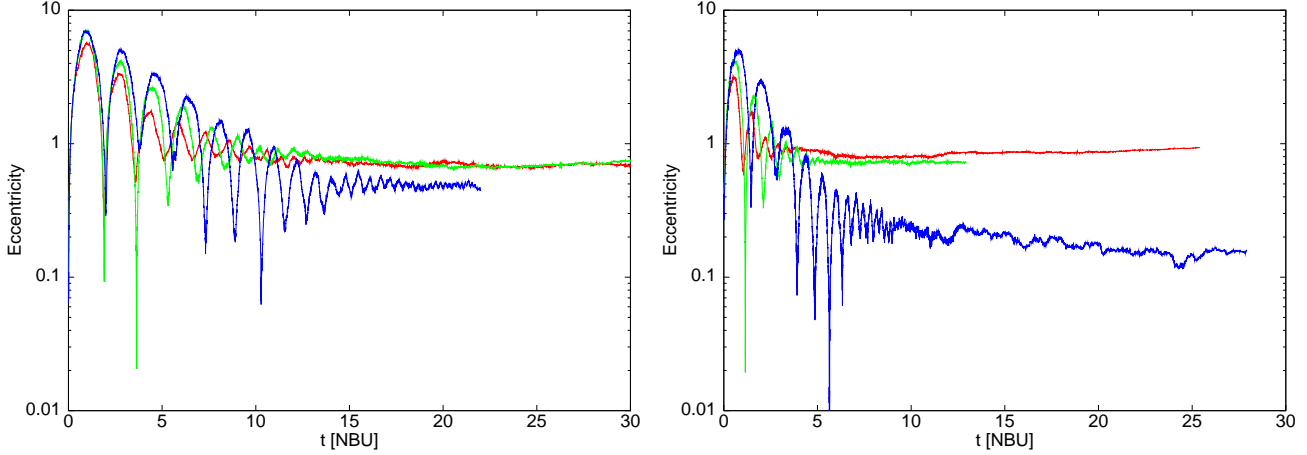


Figure 6. Influence of rotation on final eccentricities. *Left panel:* King $W_0 = 3$, models \mathcal{F} , \mathcal{C} and \mathcal{I} in green, red and blue, respectively. *Right panel:* King $W_0 = 6$, models \mathcal{O} , \mathcal{L} and \mathcal{Q} in green, red and blue, respectively. The colours indicate the different rotation parameters used in the simulations: $\omega_0 = 0.0$ red, $\omega_0 = 0.3$ green, $\omega_0 = 0.6$ blue

Set	Model	t_{stab}	\bar{e}	e_{end}	$s_{\bar{e}}$	s_e	\bar{e}_{trans}
1	\mathcal{A}	40	0.0812 [41.00;52.15]	0.0930	0.0002	0.0153	0.13 [26.4;32.7]
	\mathcal{B}	34	0.1212 [35.00;40.33]	0.1069	0.0002	0.0102	0.29 [25.1;28.8]
	\mathcal{C}	13	0.7272 [35.00;36.73]	0.7146	0.0002	0.0047	0.72 [14.7;18.0]
2	\mathcal{D}	?	0.1447 [35.00;38.96]	0.1512	0.0008	0.0348	0.14 [28.2;34.7]
	\mathcal{E}	35?	0.1239 [35.00;38.00]	0.1586	0.0005	0.0197	0.12 [24.9;32.4]
	\mathcal{F}	15	0.7135 [33.00]	0.7135	-	-	0.72 [13.3;16.9]
3	\mathcal{G}	46?	0.1714 [40.00;56.00]	0.2204	0.0005	0.0462	0.15 [32.8;42.0]
	\mathcal{H}	38	0.1206 [38.00;53.15]	0.1184	0.0003	0.0261	0.14 [23.0;29.4]
	\mathcal{I}	19	0.4497 [22.00]	0.4497	-	-	0.50 [14.9;18.9]
4	\mathcal{J}	15	0.1369 [22.00;30.46]	0.1349	0.0003	0.0170	0.25 [8.3;11.6]
	\mathcal{K}	14	0.2517 [22.00;28.84]	0.2607	0.0004	0.0228	0.13 [7.1;9.4]
	\mathcal{L}	3	0.9116 [22.00;25.41]	0.9359	0.0003	0.0127	0.90 [5.7;7.6]
5	\mathcal{M}	?	0.1558 [18.38]	0.1558	-	-	0.26 [12.1;14.1]
	\mathcal{N}	16	0.0387 [22.00;30.58]	0.0878	0.0003	0.0191	0.19 [8.8;11.6]
	\mathcal{O}	5	0.7276 [12.95]	0.7276	-	-	0.71 [5.8;7.0]
6	\mathcal{P}	22	0.0914 [25.00;26.47]	0.0813	0.0003	0.0073	0.07 [12.1;16.0]
	\mathcal{Q}	13	0.1534 [25.00;27.90]	0.1599	0.0002	0.0075	0.25 [6.7;8.3]

Table 3. Compiled data of eccentricity evolution for the complete set of simulations. t_{stab} represents the time when the eccentricity remains passably constant, \bar{e} is the average eccentricity measured over the time interval mentioned below, e_{end} the value at the end of the simulation. Disregarding appearing drifts, errors were calculated based on an 0.002 step-width output considering the same time intervals; s_e is the error of the single value and \bar{e}_{trans} the error of the mean value eccentricity. \bar{e}_{trans} is an average eccentricity over the epoch when the system turns to a constant energy loss rate

6 BROWNIAN MOTION

The centre of mass (CM) of a hardened binary is expected to perform an irregular motion in the central region of the stellar system. This motion is often described by the concept of Brownian motion, as it is characterised by a friction force (dynamical friction) and a fluctuating force (as the result of scattering events and encounters of field stars). Applying energy equipartition in thermodynamic equilibrium, the mean square velocity of the CM of the binary $\langle v_{\text{CM}}^2 \rangle$ is connected to the mean square velocity of the central field stars $\langle v_*^2 \rangle$ by

$$\langle v_{\text{CM}}^2 \rangle = \frac{m_*}{M_{2\text{BH}}} \langle v_*^2 \rangle \quad (11)$$

where $M_{2\text{BH}}$ is the sum of the black hole masses.

However, the irregular motion of the CM is to be distinguished from the movement of a single massive particle since the binding energy of the binary changes due to (super-elastic) scattering events. The characteristics of the Brownian motion of a massive black hole binary have been discussed in detail by Merritt (2001), where $\langle v_{\text{CM}}^2 \rangle$ is expected to be increased by a factor $\lesssim 2$, allowing for the higher recoil velocities of a binary after super-elastic scattering of field stars and for the decreased dynamical friction force on the CM, since the trajectories of the field stars are randomly orientated in direction after such a process.

The CM motion was investigated for a series of King parameters. Fig.9 displays the CM movement during the whole simulation time for King potential $W_0 = 6$, applying rota-

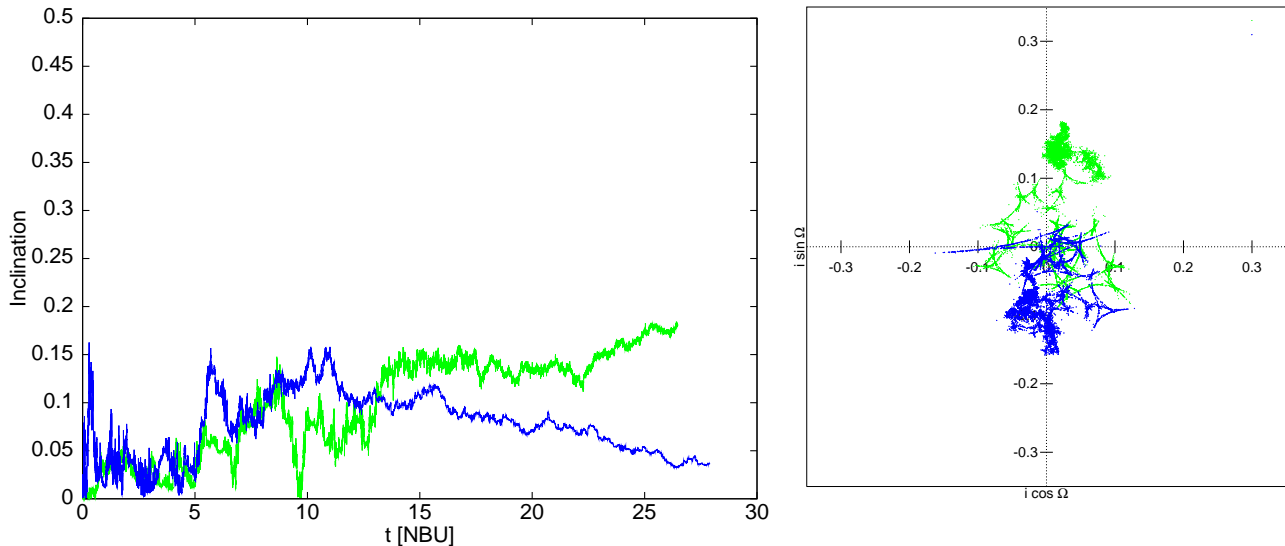


Figure 7. *Left panel:* Evolution of the inclination for models \mathcal{P} (green) and \mathcal{Q} (blue) *Right panel:* Positions of the angular momentum vector in a polar representation for the same models

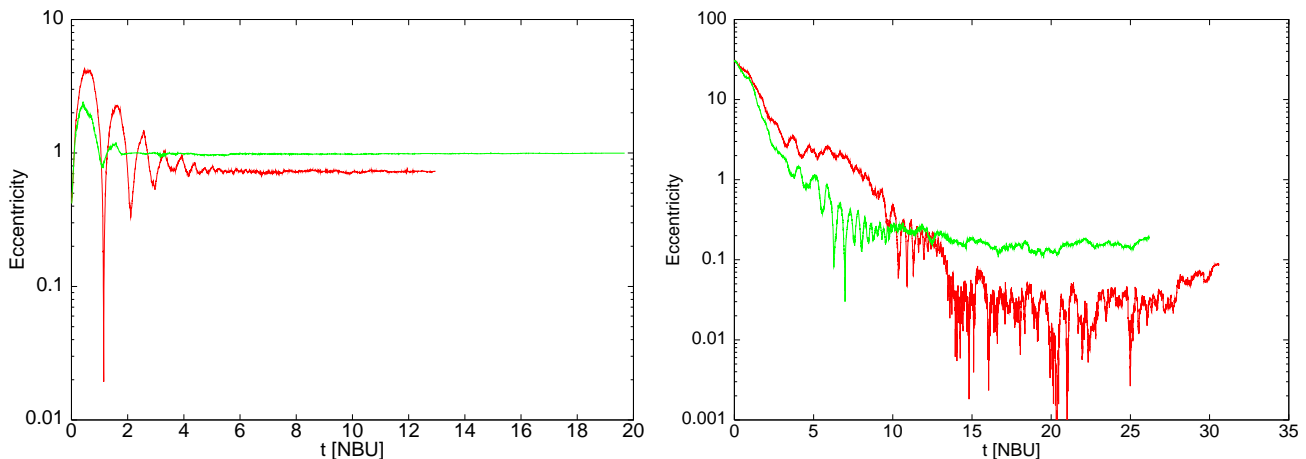


Figure 8. *Left panel:* Influence of rotation and counter-rotation on the evolution of the eccentricity of the IMBHs. The upper curve (at later times, green in the on-line version of the article) corresponds to model \mathcal{O} , for IMBHs initially set up to be counter-rotating; the lower curve (red colour) is the same model with co-rotation of the IMBHs. *Right panel:* Same-same for model \mathcal{N}

tion parameters $\omega_0 = 0.0$ and $\omega_0 = 0.6$, both with an initial IMBH velocity $v_0 = 0.136v_c$. A color gradient plot of the CM trajectory has been used to give an impression of the temporal evolution. In the absence of rotation $\omega_0 = 0.0$, the characteristics of a rather irregular motion appears, while with rotation $\omega_0 = 0.6$, a turning motion of the CM occurs. This motion seems to follow the rotation of the stellar system.

Elevated values of the CM mean velocity were found in all simulations, quantified by the ratio $\langle v_{\text{CM}}^2 \rangle / \langle v_{\text{equ}}^2 \rangle$ with $\langle v_{\text{equ}}^2 \rangle = (m_*/M_{2\text{BH}})\sigma_0^2$. The results of three simulations are shown in Tab.5. The postulated factor $\lesssim 2$ is manifestly exceeded even without rotation, but may be smaller if a change of the central stellar velocity dispersion σ is taken into account, while calculations here are based on the initial value σ_0 within the 1% Lagrangian radius of the stellar model. Nevertheless, a time evolution of the mean square velocity indicated that a constant value was not yet reached

at the end of the simulations but may have grown larger if runs had been continued.

7 GRAVITATIONAL WAVES: DETECTABILITY OF THE SYSTEMS WITH LISA

7.1 Post evolution of the binary of IMBHs

The advantage of direct-summation codes, accuracy, is at the price of performance. We have chosen N -body in order to investigate this problem but in order to analyse the ulterior evolution of the binary down to a GW frequency observable by LISA, we have to resort to alternative schemes. If we were to integrate the binary system until the orbital period of the binary is within the range of observations of LISA, we would have to leave the simulations running for months. This is not desirable for obvious

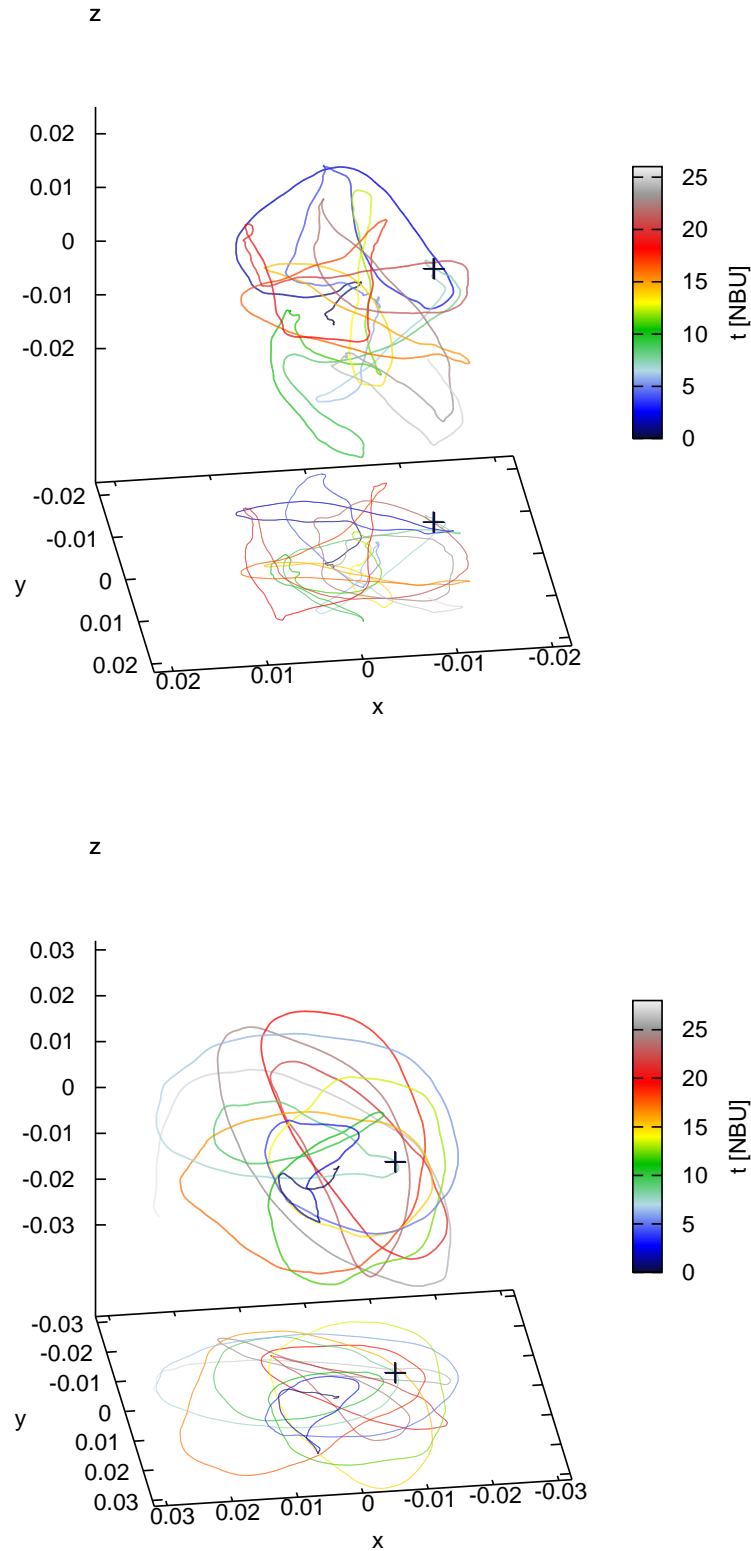


Figure 9. *Upper panel:* Centre-of-mass trajectory of model \mathcal{L} ($\omega_0 = 0.0$). *Lower panel:* Same for model \mathcal{Q} ($\omega_0 = 0.6$) The cross indicates the moment in which there is a constant energy loss rate ($t \sim 7.6$ for $\omega_0 = 0.0$ and $t \sim 8.4$ for $\omega_0 = 0.6$)

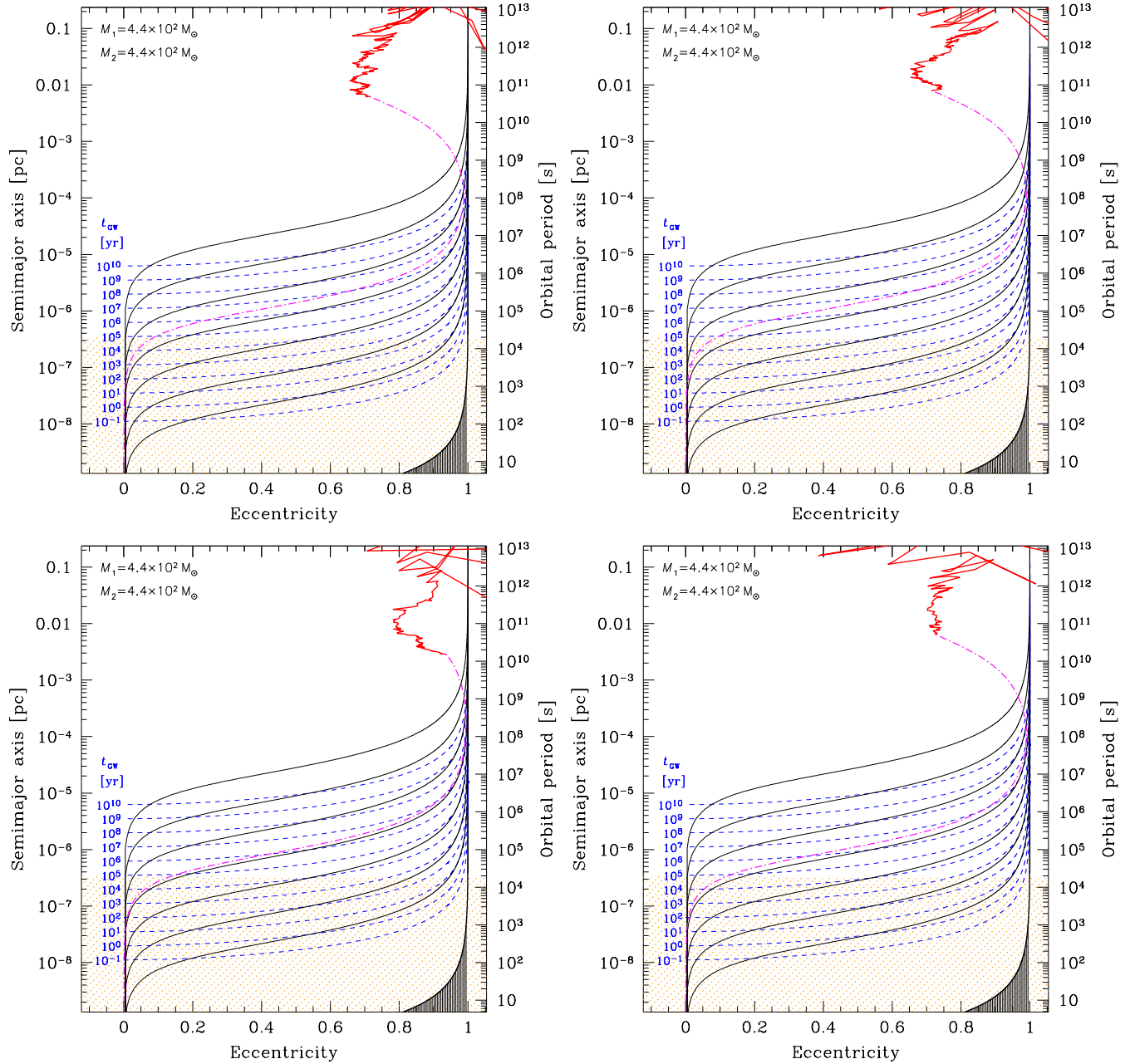


Figure 10. Inspiral of the IMBH binary of Models *C*, *F*, *L* and *O* from the top to the bottom and from the left to the right. We show in this figure the evolution of the binary in the eccentricity–semi-major axis plane. The zigzag curves (red in the on-line version) depict the results of the N –body simulations. Initially the IMBHs do not constitute a bound system and therefore the eccentricity of the system is ill-defined, as explained at the beginning of Section (4.1). This is causing the initial values of e become > 1 . We then make a semi-analytical expansion of the evolution starting from the last point in the numerical simulations (dot-dashed curve, magenta in the on-line version of the paper) by taking into account the Physical properties of the system at that moment: semi-major axis, eccentricity, velocity dispersion of the stellar system and stellar density, as shown in Table 6. Thus, we evolve the binaries until they enter the LISA bandwidth, which we depict as a lightly shaded area (orange in the on-line version). The black solid curves correspond to the trajectories due only to the emission of GWs (Peters 1964) and we additionally show the corresponding inspiral t_{GW} for 10^{10} yrs, 10^9 yrs etc. As shown in (Amaro-Seoane & Freitag 2006), one recovers partially the N –body results with the semi-analytical approach if one starts at a previous point in the curve corresponding to the numerical simulation. The black-shaded region on the right corresponds to the last stable circular orbit.

reasons. Instead, we recur to a semi-analytical method to evolve the orbital elements of the binary taking into account the dynamics and the GW emission of the system, as introduced in Amaro-Seoane & Freitag (2006): we stop the direct-summation calculation after the initial strong fluctu-

ating phase; when the eccentricity achieves a *steady* value. In order to locate in the LISA bandwidth the position of the binary, we employ the results of the direct-summation simulation and extend them with a semi-analytical method. The dynamics will, in general, tend to increase the eccentricity,

Model	i_{\max}	\bar{i}
\mathcal{A}	0.191 [37.151]	0.14 [32.7;52.2]
\mathcal{B}	0.360 [19.275]	0.27 [28.8;40.3]
\mathcal{C}	0.362 [3.316]	0.23 [18.0;36.7]
\mathcal{D}	0.271 [18.557]	0.04 [34.7;39.0]
\mathcal{E}	0.289 [12.836]	0.21 [32.4;38.0]
\mathcal{F}	0.352 [3.329]	0.07 [16.9;33.0]
\mathcal{G}	0.189 [24.961]	0.14 [42.0;56.0]
\mathcal{H}	0.201 [23.056]	0.13 [29.4;53.2]
\mathcal{I}	0.344 [1.686]	0.12 [18.9;22.0]
\mathcal{J}	0.316 [15.869]	0.24 [11.6;30.5]d
\mathcal{K}	0.252 [7.138]	0.18 [9.4;28.8]
\mathcal{L}	0.867 [20.895]	0.72 [7.6;25.4]
\mathcal{M}	0.349 [11.120]	0.24 [14.1;18.4]
\mathcal{N}	0.178 [9.546]	0.07 [11.6;30.6]
\mathcal{O}	0.492 [5.202]	0.42 [7.0;13.0]
\mathcal{P}	0.184 [26.423]	0.15 [16.0;26.5]
\mathcal{Q}	0.158 [10.150]	0.09 [8.3;27.9]d

Table 4. Inclination characteristics regarding all simulations. i_{\max} denotes the maximum value at the mentioned time unit, \bar{i} is the mean value over the mentioned time interval, which ranges from the time unit when a constant energy loss rate occurs until the end of the simulation. The mean values are calculated despite some runs showing drift, in which case they are indicated with a "d".

Model	$\langle v_{\text{CM}}^2 \rangle$	$\langle v_{\text{equ}}^2 \rangle$	$\langle v_{\text{CM}}^2 \rangle / \langle v_{\text{equ}}^2 \rangle$
\mathcal{L}	$1.33 \cdot 10^{-3}$	$3.73 \cdot 10^{-4}$	3.5
\mathcal{N}	$2.79 \cdot 10^{-3}$	$3.66 \cdot 10^{-4}$	7.6
\mathcal{Q}	$2.18 \cdot 10^{-3}$	$3.32 \cdot 10^{-4}$	6.6

Table 5. Mean square velocities for the CM of the binary ($\langle v_{\text{CM}}^2 \rangle$) compared to the equilibrium mean square velocity ($\langle v_{\text{equ}}^2 \rangle$) of a single particle, for some simulations. The $\langle v_{\text{CM}}^2 \rangle$ were calculated over the blue epochs of section (9) and over [11.60;30.58] in the case $W_0 = 6$, $\omega_0 = 0.3$, $v_0 = v_c$.

whilst the emission of GWs circularises the orbit. These two processes are competitive. The basic idea to further evolve the binary is to split the evolution of both the semi-major axis and the eccentricity in two contributions, one driven by the dynamical interactions with stars (subscript *dyn*) and another by the emission of GWs (subscript *GW*),

$$\frac{da}{dt} = \left(\frac{da}{dt}\right)_{\text{dyn}} + \left(\frac{da}{dt}\right)_{\text{GW}}, \quad \frac{de}{dt} = \left(\frac{de}{dt}\right)_{\text{dyn}} + \left(\frac{de}{dt}\right)_{\text{GW}} \quad (12)$$

The *GW* terms are as given by the approach used in Peters (1964). As for the dynamical part, we resort to the scheme described in Quinlan (1996). For more details about this approach, see Section 3 of Amaro-Seoane & Freitag (2006).

In Fig.(10) we depict the results of this approach for the models \mathcal{C} , \mathcal{F} , \mathcal{L} and \mathcal{O} . We have chosen them for being the most interesting ones from a dynamical point of view, since they have the largest eccentricities by the moment of entrance in the observatory’s sensitivity window. Also, from the standpoint of detectability, these are the most challeng-

ing ones due to the same reason. We can see that in all four models the binary of IMBHs enters the bandwidth with a residual eccentricity which, even if rather mild, is not negligible, from the point of view of detection.

7.2 Event rates

Fregeau et al. (2006) estimated the detection of binary IMBHs by LISA for the single cluster channel. They assumed that any cluster undergoing a collisional runaway, such as those found in the Monte Carlo numerical simulations of Gürkan et al. (2006), form a two very massive stars. These evolve separately and eventually may collapse and build two IMBHs separately, so that the IMBHs do *not* coalesce in the process of their formation, but are born independently.

Amaro-Seoane & Freitag (2006) calculated the event rate for formation of binaries of IMBHs based on the results of Fregeau et al. (2006) in the scenario of two colliding clusters, the double cluster channel (see their Section 4, also for a more detailed explanation of the following events). Their work assumed that the IMBHs were already present at the centres of the two clusters undergoing the crash. When the two clusters merge, the IMBHs are drawn to the centre due to dynamical friction and constitute a binary which eventually coalesce. The difference in the calculation of event rates of Amaro-Seoane & Freitag (2006) and Fregeau et al. (2006) is the number of IMBHs formed per cluster and the requirement for the host clusters to merge.

In both estimations, the probability that a cluster evolves to the runaway phase was set to 0.1 as an illustrative case, though it can be as high as 0.5 (Freitag et al. 2006b). Both works assumed that a runaway always leads to the formation of an IMBH. We refer the reader to Section 4 of Amaro-Seoane & Freitag (2006) and Fregeau et al. (2006) for a detailed explanation and exposition of the uncertainties in the calculations. To summarise, the Fregeau et al. (2006) results for the LISA detector are

$$\Gamma_{\text{Freg}}|_{\text{opt}} \in [200, 250] \text{ yr}^{-1} \quad (13)$$

$$\Gamma_{\text{Freg}}|_{\text{pes}} \in [40, 50] \text{ yr}^{-1}.$$

Where the subscript “Freg” stands for Fregeau et al. (2006), the subscript “opt” for the optimistic estimation, assuming that the probability for a cluster evolving to the runaway stage is 0.5, and the subscript “pes” stands for pesimistic, which is the result of using 0.1 instead. Amaro-Seoane & Freitag (2006) find the following results, where we use a nomenclature similar as above and set the probability for the host clusters to merge to 1 (these would decrease by a factor 10 if one was to use 0.1 instead, see discussion about the “UCDG channel” in their work)

$$\Gamma_{\text{ASF}}|_{\text{opt}} \in [100, 125] \text{ yr}^{-1} \quad (14)$$

$$\Gamma_{\text{ASF}}|_{\text{pes}} \in [4, 5] \text{ yr}^{-1}.$$

So that the contribution to the total number of binaries of IMBHs from both channels is

$$\Gamma_{\text{tot}}|_{\text{opt}} \in [300, 375] \text{ yr}^{-1} \quad (15)$$

$$\Gamma_{\text{tot}}|_{\text{pes}} \in [44, 55] \text{ yr}^{-1}$$

Simulation	Time	R_c	N	σ_R^2	σ_T^2	σ_{tot}	n	\bar{m}	ρ	ρ^*	σ_{tot}^*
\mathcal{C}	36.0	0.376	7778	0.255	0.304	0.929	34878.9	$1.82 * 10^{-5}$	0.635	0.544	0.860
\mathcal{F}	33.0	0.376	7627	0.253	0.261	0.880	34201.8	$1.82 * 10^{-5}$	0.622	0.534	0.943
\mathcal{L}	25.0	0.216	4209	0.476	0.782	1.428	99739.3	$2.03 * 10^{-5}$	2.025	1.555	1.575
\mathcal{O}	12.0	0.223	4270	0.383	0.265	0.956	91828.0	$2.03 * 10^{-5}$	1.864	1.433	0.967

Table 6. All values are given in N -body units. In the table R_c is the core radius, N the number of stars within the core radius, including the two IMBHs, σ_R^2 the radial velocity dispersion (squared), σ_T^2 the tangential velocity dispersion (squared, 1D), $\sigma_{tot} = \sqrt{\sigma_R^2 + 2\sigma_T^2}$ the velocity dispersion (3D, including IMBHs), n the particle density within the core radius (including IMBHs), \bar{m} the average particle mass within the core radius (including IMBHs), ρ the average mass density within the core radius (including IMBHs), ρ^* the average mass density within the core radius (excluding IMBHs), σ_{tot}^* the velocity dispersion within the core radius (3D, excluding 2BH)

Or, in the unlikely very pessimistic situation of having the host clusters to merge with a 0.1 probability, we have the following “optimistic–pessimistic” and “pessimistic–pessimistic” results

$$\begin{aligned} \Gamma_{tot}^{|\text{opt}}^{\text{pes}} &\in [210, 262.5] \text{ yr}^{-1} \\ \Gamma_{tot}^{|\text{pes}}^{\text{pes}} &\in [40.4, 50.5] \text{ yr}^{-1} \end{aligned} \quad (16)$$

These results are encouraging enough that we address the parameter estimation of the sources. We describe the methods and results in the next sections.

7.3 The gravitational waveform

To investigate the detectability of these sources for LISA, we use the restricted post-Newtonian (PN) approximation for the GW, where we assume 2-PN corrections to both the conservative and adiabatic dynamics of the system, but conserve the amplitude at the dominant Newtonian order. With this in mind, the waveform polarisations for non-spinning eccentric binaries at the detector are given by (in units of $G = c = 1$) (Damour et al (2004))

$$\begin{aligned} h_+(t) &= \frac{M\eta}{D_L} \left\{ (1 + \cos^2 \iota) \left[\cos 2\varphi \left(-\dot{r}^2 + r^2 \dot{\varphi}^2 + \frac{M}{r} \right) \right. \right. \\ &\quad \left. \left. + 2r \dot{r} \dot{\varphi} \sin 2\varphi \right] + \left(-\dot{r}^2 - r^2 \dot{\varphi}^2 + \frac{M}{r} \right) \sin^2 \iota \right\} \\ h_\times(t) &= -\frac{2M\eta}{D_L} \cos \iota \left\{ \left(-\dot{r}^2 + r^2 \dot{\varphi}^2 + \frac{M}{r} \right) \sin 2\varphi \right. \\ &\quad \left. - 2r \dot{r} \dot{\varphi} \cos 2\varphi \right\}, \end{aligned} \quad (17)$$

$$(18)$$

where $\cos \iota = \hat{\mathbf{L}} \cdot \hat{\mathbf{n}}$. Here, $\hat{\mathbf{L}}$ is the direction of the binary’s orbital angular momentum and $\hat{\mathbf{n}}$ is the direction from the observer to the source (such that the GWs propagate in the $-\hat{\mathbf{n}}$ direction). M is the total mass of the system, $\eta = M_1 M_2 / M^2$ is the symmetric mass ratio and D_L is the luminosity distance to the source. The components (r, φ) denote the orbital radius and phase of the system (also referred to as the true anomaly), and are schematically described by the equations (Hinder et al (2008))

$$r/M = r_{0\text{PN}} x^{-1} + r_{1\text{PN}} + r_{2\text{PN}} x + \mathcal{O}(x^2) \quad (19)$$

$$M\dot{\varphi} = \dot{\varphi}_{0\text{PN}} x^{3/2} + \dot{\varphi}_{1\text{PN}} x^{5/2} + \dot{\varphi}_{2\text{PN}} x^{7/2} + \mathcal{O}(x^{9/2}) \quad (20)$$

$$l = l_{2\text{PN}} + l_{2\text{PN}} x^2 + \mathcal{O}(x^3) \quad (21)$$

$$M\dot{l} = M\dot{n} = x^{3/2} + \dot{l}_{1\text{PN}} x^{5/2} + \dot{l}_{2\text{PN}} x^{7/2} + \mathcal{O}(x^{9/2}) \quad (22)$$

where l is the mean anomaly and $n = 2\pi/P$ is the mean motion, where P is the orbital period defined as the time to go from pericenter to pericenter. Due to precession effects, this is different from the time taken to go from φ to $\varphi + 2\pi$. The dot represents the time derivative, e.g. $\dot{\varphi} = d\varphi/dt$. We also define the invariant PN coefficient $x = (M\omega)^{2/3}$, where the angular frequency is defined as $\omega = (2\pi + \Delta\varphi)/P$ and $\Delta\varphi$ is the precession angle of the pericenter per period. We should note that the coefficients in the equations presented above and below are in general functions of the instantaneous eccentricity e and the eccentric anomaly u . In the limit of the eccentricity $e \rightarrow 0$, we reclaim the circular orbit case where $\omega = \dot{\varphi}$. The adiabatic evolution of x and e are given by

$$M\dot{x} = \dot{x}_{0\text{PN}} x^5 + \dot{x}_{1\text{PN}} x^6 + \dot{x}_{2\text{PN}} x^7 + \mathcal{O}(x^{15/2}) \quad (23)$$

$$M\dot{e} = \dot{e}_{0\text{PN}} x^4 + \dot{e}_{1\text{PN}} x^5 + \dot{e}_{2\text{PN}} x^6 + \mathcal{O}(x^{13/2}). \quad (24)$$

where we point the reader to the appendix of Hinder et al (2008) for the complete description of the above equations. The waveforms are generated as follows : after we have evolved the above equations for x and e , we numerically integrate Equation 22 to obtain $l(t)$. We then use this value to solve the post-Newtonian Kepler’s Equation 21, which is a transcendental equation in $u(t)$. Once we have $u(t), e(t)$ and $x(t)$, we can then calculate $r(t), \dot{r}(t), \varphi(t), \dot{\varphi}(t)$, where we calculate the integral of $\dot{\varphi}(t)$ and the derivative $\dot{r}(t)$ numerically.

In this work, to fully describe the GW polarisations we use the following parameter set : $\vec{\lambda} = \{\ln(M_c), \ln(\mu), \ln(D_L), \ln(a_0), \cos \theta, \phi, e_0, \cos \iota, \psi\}$, where $M_c = M\eta^{3/5}$ is the chirp-mass, $\mu = M\eta$ is the reduced mass, D_L is the luminosity distance, a_0 is the initial semi-major axis of the orbit, (θ, ϕ) are the co-latitude and longitudinal position of the source in the sky, e_0 is the initial eccentricity, ι is the inclination of the orbital plane and ψ is the GW polarisation angle.

7.4 Detector response and parameter error estimation

LISA can be thought of as pair of co-located detectors rotated with respect to each other by an angle of 45 degrees. In the Low Frequency Approximation (LFA) (Cutler 1998), we can write the individual detector responses as

$$h_i(t) = h_+(\xi(t)) F_i^+(t) + h_\times(\xi(t)) F_i^\times(t), \quad (25)$$

where $\xi(t)$ is the phase shifted time parameter defined by

$$\xi(t) = t - R_{\oplus} \sin \theta \cos(\alpha(t) - \phi). \quad (26)$$

Here R_{\oplus} corresponds to one AU and $\alpha(t) = 2\pi f_m t + \kappa$, where the LISA modulation frequency is $f_m = 1/\text{year}$ and κ is the initial ecliptic longitude of the guiding center of the LISA constellation. The functions $F^{+, \times}(t; \theta, \phi, \psi)$ are the beam pattern functions of the detector (Cornish & Rubbo (2003)).

Given sources $h(t)$ and $g(t)$ we can define a noise weighted inner product

$$\langle h | g \rangle = 2 \int_0^{\infty} \frac{df}{S_n(f)} \tilde{h}(f) \tilde{g}^*(f) + \tilde{h}^*(f) \tilde{g}(f). \quad (27)$$

where $\tilde{h}(f)$ is the Fourier transform of the signal, an asterisk denotes a complex conjugate term and $S_n(f)$ is the one-sided noise spectral density of the detector. For this study, we use a noise curve given by

$$S_n(f) = S_n^{\text{instr}}(f) + S_n^{\text{conf}}(f) \quad (28)$$

where the instrumental noise $S_n(f)$ is given by

$$S_n^{\text{instr}}(f) = \frac{1}{4L^2} \left[2S_n^{\text{pos}}(f) \left(2 + \left(\frac{f}{f_*} \right) \right) + 8S_n^{\text{acc}}(f) \right. \\ \left. \times \left(1 + \cos^2 \left(\frac{f}{f_*} \right) \right) \left(\frac{1}{(2\pi f)^4} + \frac{(2\pi 10^{-4})^2}{(2\pi f)^6} \right) \right]. \quad (29)$$

(Cornish & Rubbo 2003). Here $L = 5 \times 10^6$ km is the arm-length for LISA, $S_n^{\text{pos}}(f) = 4 \times 10^{-22} \text{ m}^2/\text{Hz}$ and $S_n^{\text{acc}}(f) = 9 \times 10^{-30} \text{ m}^2/\text{s}^4/\text{Hz}$ are the position and acceleration noises respectively. The quantity $f_* = 1/(2\pi L)$ is the mean transfer frequency for the LISA arm. Note that we have also included a reddened noise term which steepens the noise curve between 10^{-4} and 10^{-5} Hz. To model the galactic or confusion noise we use the following confusion noise estimate derived from a Nelemans, Yungelson, Zwart (NYZ) galactic foreground model (Nelemans et al 2004; Timpano et al 2006)

$$S_n^{\text{conf}}(f) = \begin{cases} 10^{-44.62} f^{-2.3} & 10^{-4} < f \leq 10^{-3} \\ 10^{-50.92} f^{-4.4} & 10^{-3} < f \leq 10^{-2.7} \\ 10^{-62.8} f^{-8.8} & 10^{-2.7} < f \leq 10^{-2.4} \\ 10^{-89.68} f^{-20} & 10^{-2.4} < f \leq 10^{-2} \end{cases}, \quad (30)$$

where the confusion noise has units of Hz^{-1} .

Using the noise weighted inner product, we can define the optimal signal to noise ratio (SNR) by

$$\langle h | h \rangle_{\text{opt}} = 4 \int_0^{\infty} \frac{df}{S_n(f)} |\tilde{h}^2(f)|. \quad (31)$$

We can also define the Fisher information matrix (FIM) by

$$\Gamma_{\alpha\beta} = \langle \partial_{\alpha} h | \partial_{\beta} h \rangle. \quad (32)$$

where the theoretical standard deviation error estimate in parameter recovery is given as

$$\sigma_{\alpha} = \sqrt{(\Gamma_{\alpha\alpha})^{-1}} \quad (33)$$

The derivatives of the waveforms appearing in the FIM are generated numerically. We refer the reader to (Porter & Cornish 2008) for the intricacies in the numerical calculation of the FIM.

7.5 Sampling the parameter space

Figure 10 provides the semi-major axes, eccentricities and orbital periods for the models \mathcal{C} , \mathcal{F} , \mathcal{L} and \mathcal{O} , assuming an equal mass IMBH binary with individual rest-frame masses of $M_i = 440 M_{\odot}$. To sample the parameter space we ran a 1000 iteration Monte Carlo simulation over the parameters $\{a_0, e_0, \theta, \phi, \iota, \psi\}$, while keeping the luminosity distance and redshifted mass parameters constant. For the angular parameters we assume $(\cos \theta, \cos \iota) \in [-1, 1]$ and $(\phi, \psi) \in [0, 2\pi]$ and we then draw uniformly from these ranges.

As the IMBHs in the study are quite low mass as compared to SMBHs, we need to ensure that the sources are detectable. Given the masses of the systems in question, the GW frequency at the last stable circular orbit is between 4-6 Hz, which is well outside the frequency range of LISA. Therefore, we placed all sources at a common distance of $D_L = 100$ Mpc and required a SNR greater than 5. At this distance, the parameter values observed by LISA are the redshifted rather than rest frame values. To account for this, the measured total mass is $M(z) = (1+z)M$ and the measured GW frequency of the waveform is $f_{\text{gw}}(z) = f_{\text{gw}}/(1+z)$. In this study we use the following relation between redshift, z , and luminosity distance, D_L :

$$D_L = \frac{c(1+z)}{H_0} \int_0^z dz' \left[\Omega_R (1+z')^4 + \Omega_M (1+z')^3 + \Omega_{\Lambda} \right]^{-1/2}, \quad (34)$$

where we assume WMAP values of values of $(\Omega_R, \Omega_M, \Omega_{\Lambda}) = (4.9 \times 10^{-5}, 0.27, 0.73)$ and a Hubble's constant of $H_0 = 71$ km/s/Mpc.

We also decided to enforce a maximum possible GW frequency of 3 mHz to ensure the fidelity of the LFA (Cornish & Rubbo 2003; Shapiro Key & Cornish 2009). Thus, using the information in Figure 11, we evolved the sources from first entering the LISA bandwidth to the point where they achieved the required SNR threshold. For this we assumed a 3 year mission lifetime for LISA.

Using the above constraints it was possible to find minimum and maximum values of (a_0, e_0) which satisfied both the SNR and maximum frequency constraints. Furthermore to sample this parameter sub-space we found it was possible to relate the eccentricity and semi-major axis for the four models according to a quadratic law, i.e.

$$e = -c_0 + c_1 a_0 + c_2 a_0^2, \quad (35)$$

where we provide the coefficients c_i , the maximum and minimum values of both a_0 and e_0 in Table 7. Thus, by uniformly sampling a_0 , we also have a corresponding sample in e_0 . We can see from Table 7 that although the binaries have appreciable eccentricities when they first enter the LISA band, i.e. $e \sim 0.1 - 0.15$, by time the systems become observable the eccentricity has dropped to $e \sim 0.012 - 0.019$.

While the Monte Carlo is carried out using the sky coordinates of the source, a more interesting quantity to quote is LISA's angular resolution for each source. We define the angular resolution as

$$\Delta\Omega = 2\pi \sqrt{\Sigma^{\theta\theta} \Sigma^{\phi\phi} - (\Sigma^{\theta\phi})^2}, \quad (36)$$

where

Model	c_0	c_1	c_2	$a_0^{\min} \times 10^{-8} pc$	$a_0^{\max} \times 10^{-8} pc$	e_0^{\min}	e_0^{\max}
\mathcal{C}	1.1366×10^{-3}	9.6414×10^4	9.4069×10^{11}	3.6123	10.669	3.5924×10^{-3}	1.9942×10^{-2}
\mathcal{F}	6.9767×10^{-4}	6.3737×10^4	6.9846×10^{11}	3.6107	9.8673	2.5227×10^{-3}	1.2389×10^{-2}
\mathcal{L}	1.1591×10^{-3}	1.0606×10^5	1.1698×10^{12}	3.7049	9.3739	4.3852×10^{-3}	1.9056×10^{-2}
\mathcal{O}	8.6073×10^{-4}	8.4893×10^4	1.0181×10^{12}	3.8524	9.0204	3.9227×10^{-3}	1.5081×10^{-2}

Table 7. Quadratic power law coefficients for the four models $\mathcal{C}, \mathcal{F}, \mathcal{L}, \mathcal{O}$, as well as minimum and maximum ranges for the initial semi-major axes a_0 and eccentricity e_0 .

$$\Sigma^{\alpha\beta} = \langle \Delta\lambda^\alpha \Delta\lambda^\beta \rangle = (\Gamma_{\alpha\beta})^{-1}. \quad (37)$$

We can now define the quantities appearing in the angular resolution as $\Sigma^{\theta\theta} = \langle \Delta \cos \theta \Delta \cos \theta \rangle$, $\Sigma^{\phi\phi} = \langle \Delta \phi \Delta \phi \rangle$ and $\Sigma^{\theta\phi} = \langle \Delta \cos \theta \Delta \phi \rangle$. The angular resolution has units of steradians.

7.6 Results of the Monte Carlo

In Figure 11 we plot the recovered SNRs for the four models of IMBH inspiral. The models $\mathcal{C}, \mathcal{F}, \mathcal{L}$ and \mathcal{O} are represented top to bottom, and left to right. We can see that while it is possible to have strong sources, with SNRs ≥ 300 , the vast majority of samples returned more modest, but detectable SNRs in the range of 5 to 50. This means that IMBH inspirals should be observable with the LISA detector.

Due to the lower mass ranges of these binaries, for systems placed at 100 Mpc, the sources start to become visible in the detector at GW frequencies of 5×10^{-4} Hz and higher. However, as they are still very widely separated at this point, there is very little evolution in frequency or eccentricity over a three year period. In Figure 12 we plot the initial and final eccentricity distributions for the four models. We can see that there is very little circularisation of the binaries during the observation period, which means that systems entering the observable LISA band with eccentricities of ~ 0.02 will reach the end of the three years with almost the same eccentricity. As a consequence, these sources should retain a measurable eccentricity throughout the LISA mission lifetime. We discuss about the consequences of these results on lower-frequency Astrophysics and Data Analysis in the next section.

8 CONCLUSIONS

In this study we have carried out a dynamical study and a first step analysis of the detection of IMBH binary systems in rotating clusters. For the case of a rotating King model without rotation, the results of the presented survey verify previous outcomes by Makino et al (1993), Hemsendorf et al (2002) for massive black hole binary evolution in Plummer models facing the development of the binding energy, the eccentricity and determined hardening constants. Analysing an extensive number of simulations, the main results from our study of the Dynamics of these systems can be described: (1) The final eccentricity is strongly dependent on the initial black hole velocities. (2) The eccentricity is dependent on the rotation parameter of the model. (3) Determined hardening rates in the same range of previous direct N -body

simulations of comparable particle numbers. (4) Only weak changes in the inclination and in the orientation of the angular momentum vector direction have been observed, consistent with simulations by Milosavljević & Merritt (2001). (5) Counter rotation simulations yield noticeable different results in eccentricity, in one case actually an extreme large value $\bar{e} = 0.997$. (6) Brownian motion of the centre of mass of the binary is influenced by the rotation of the stellar system. All simulations indicate that the orbital parameters eccentricity and inclination develop to passably constant values in the non- or only weak bound state, determined by initial conditions and the influence of dynamical friction.

In order to understand the impact of these sources in lower-frequency GW Astrophysics, we have extended the direct N -body simulations with a simplified semi-analytical model. Whilst this approach is a “kludge” and can only be envisaged as an approximation, the integration of the system down to LISA’s window is out of question because this would require months of CPU calculation and, on the top of that, the numerical error would accumulate, so that the results would not be as robust as what one can expect from direct-summation schemes.

We choose the systems yielding a larger eccentricity in the dynamical simulations because these are the most appealing cases in the sense that their detection will be very challenging. Also, information about the previous dynamical story of the system is encoded in the radiation in the form of a nonnegligible eccentricity.

The results presented above show that LISA should have no problems in identifying the existence of IMBH binaries. Such events are important for LISA data analysis as they are a previously unconsidered source in terms of detectability and parameter extraction. Our simulations also suggest that they will spend their lifetime in the detector with a measurable eccentricity. In this work, we have looked at a particular case study where the masses and the luminosity distance of the sources were fixed, and a Monte Carlo randomisation carried out over the other response parameters. We demonstrated that we will be able to accurately measure the masses and sky resolution of such sources. While the eccentricity is weak when the source becomes observable in the detector, it should still be possible to carry out a precise measurement of the initial eccentricity of the source.

For this we used the LFA response for the LISA detector. This limited the sources we investigated to a maximum GW frequency of 3 mHz to ensure that the LFA was still valid. As these are also quite high frequency sources, they have a long generation time, which puts a time constraint of the size of the Monte Carlo that can be carried out. Finally, the waveforms used in this work represent eccentric non-spinning binaries.

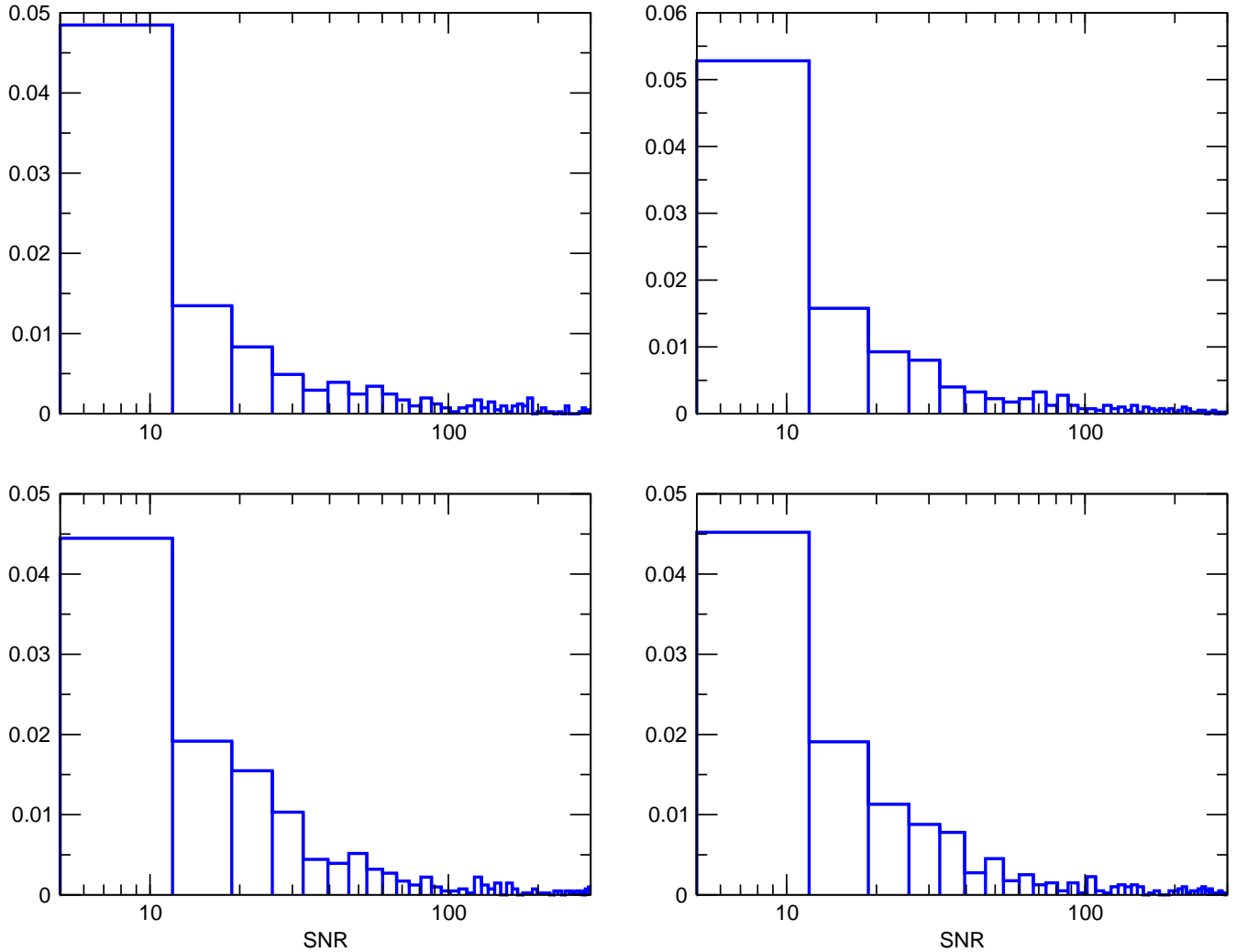


Figure 11. The optimal SNRs for the inspiral of IMBH binary of Models \mathcal{C} , \mathcal{F} , \mathcal{L} and \mathcal{O} from the top to the bottom and from the left to the right. While it is possible to have very strong sources with SNRs in the range of 300-400, the vast majority of samples return SNRs of between 5 and 50 for all four models

$\Delta\vec{\lambda}$	\mathcal{C}	\mathcal{F}	\mathcal{L}	\mathcal{O}
$\Delta M_c/M_c$	2.6982×10^{-4}	1.9155×10^{-4}	8.4848×10^{-5}	1.3321×10^{-4}
$\Delta\mu/\mu$	3.2393×10^{-3}	2.6694×10^{-3}	9.9361×10^{-4}	1.5502×10^{-3}
$\Delta D_L/D_L$	5.1611×10^{-1}	4.1823×10^{-1}	2.8644×10^{-1}	3.3223×10^{-1}
$\Delta\Omega$	2.1022×10^{-3}	1.7114×10^{-3}	9.4282×10^{-4}	1.1711×10^{-3}
$\Delta \cos \iota$	1.8954×10^{-1}	1.5333×10^{-1}	9.0724×10^{-2}	1.1194×10^{-1}
Δe_0	7.9722×10^{-7}	7.0795×10^{-7}	5.9972×10^{-7}	6.0454×10^{-7}
SNR	10.81	12.68	17.86	15.31

Table 8. Median values of the parameter estimation errors and SNRs for the four models \mathcal{C} , \mathcal{F} , \mathcal{L} , \mathcal{O} . Note that the units of $\Delta\Omega$ is steradians

As well as detectability, the extraction of the system parameters is also of great importance in GW Astrophysics. Using the FIM, we obtained the error predictions for the important system parameters. As the error predictions are a function of the position of the source in the sky, plus the orientation of the system with respect to the LISA constellation, the Monte Carlo simulations produced error distributions with large tails. Because of this fact, we have decided

to quote the median errors for the relevant parameters. In Table 8 we present the median errors for the parameters (M_c , μ , D_L , $\Delta\Omega$, $\cos \iota$, e_0). We can see that for all models the fractional errors in the estimation of the chirp-mass and reduced mass are of the order of 10^{-4} and 10^{-3} . While there is not much frequency evolution for these sources, the fact that they appear in the detector at frequencies on the order of mHz means that we can obtain errors in the luminosity

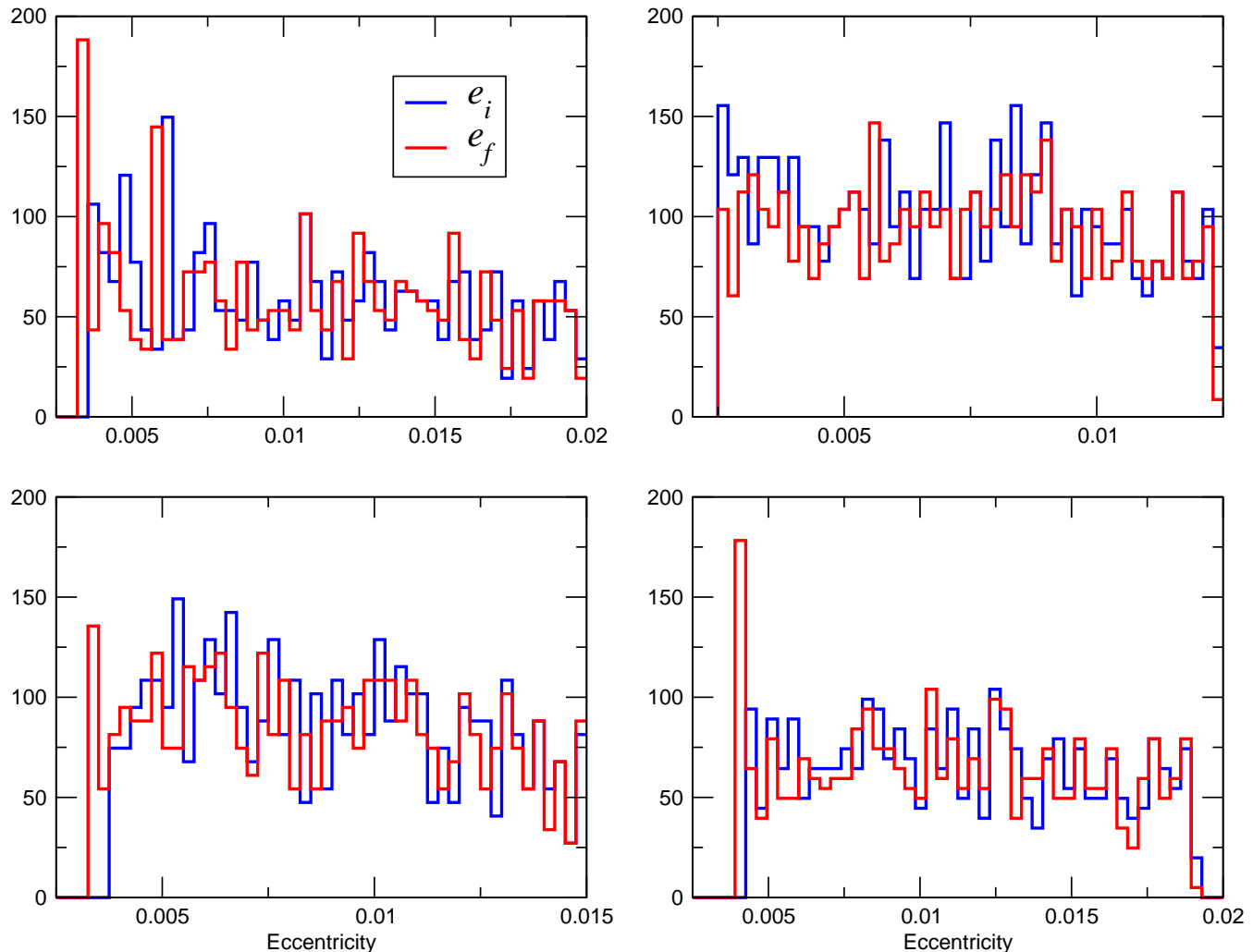


Figure 12. The initial and final eccentricities for the inspiral of IMBH binary of Models \mathcal{C} , \mathcal{F} , \mathcal{L} and \mathcal{O} from the top to the bottom and from the left to the right, assuming a 3 year observation period for LISA. As the binary components are still quite widely separated, there is little circularisation during the observation period, and the binaries thus retain a measurable eccentricity. Note the different eccentricity scales in the different cells

distance of the order of 10^{-1} . We see a similar order of error in the estimation of $\cos \iota$ which is in general a difficult quantity to measure using electromagnetic information.

It is also quite remarkable to see that angular resolution of the IMBH inspirals is very good, with median errors on the order of 10^{-3} steradians, corresponding to an error box on the sky of about 3 square degrees. This level of accuracy would place an inspiralling IMBH firmly in the field of view of a future detector such as the Large Synoptic Survey Telescope (LSST). Finally, we can also see, again from the fact that these sources are emitting GWs at frequencies on the order of mHz, the fractional errors in the estimation of initial eccentricity is on the order of 10^{-7} .

While we have shown that these IMBH binaries are detectable, there are a number of ways in which the analysis can be improved in the future. Firstly, a more representative study would also have randomised the individual masses of the binaries, as well as their luminosity distance. This would allow us to give a more concrete statement on detection and parameter estimation with the LISA detec-

tor. Secondly, we restricted the maximum GW frequency of the binary to 3 mHz to ensure a valid approximation to the LISA response. In the future, we could investigate higher frequency binaries by either using a Rigid Adiabatic Approximation (Rubbo et al 2004) or full response to the LISA detector. However, we should point out that for the higher frequency binaries, the initial eccentricity drops off rapidly, and these binaries may now be essentially circular. A more realistic study would also include the use of more realistic waveforms which include spins and higher harmonics. However, work on such templates has yet to fully start in earnest. Finally, it would also be interesting to carry out a longer Monte Carlo, and assume different mission lifetimes to see how detectability changes over observation time.

ACKNOWLEDGEMENTS

PAS is thankful to Miguel Preto for his help with the `rotinit` subroutine to create the initial conditions of the models. The work of PAS has been supported by the Deutsche

Zentrum für Luft- und Raumfahrt at the Max-Planck Institut für Gravitationsphysik (Albert Einstein-Institut) and by the Ministerio de Educación y Ciencia at the Institut de Ciències de l'Espai, IEEC/CSIC. PAS and EKP acknowledge the support of the Aspen Center for Physics for the invitation in 2008. The simulations were partially performed at the cluster TUFFSTEIN located at the AEI. PAS, EC and RS acknowledge computing time on the GRACE cluster in Heidelberg (Grants I/80 041-043 of the Volkswagen Foundation and 823.219-439/30 and /36 of the Ministry of Science, Research and the Arts of Baden-Württemberg) The work was partially supported German Science Foundation under SFB439 "Galaxies in the Young Universe" and the Volkswagen Foundation.

REFERENCES

- Aarseth, S., 2003, *Gravitational N-body simulations* (Cambridge University Press, Cambridge), p.173
- Ahmad A., Cohen L., *Journal of Computational Physics* 1973, 12, 349
- Amaro-Seoane, P. and Freitag, M., 2006, *ApJ Letts.* L53-L56
- Amaro-Seoane P., Miller M. C., Freitag M., 2009, *ApJ Lett.*, 692, L50
- Begelman M.C., Blandford R.D., Rees M.J., 1980, *Nature*, 287, 307
- Berczik P., Merritt D., Spurzem R., 2005, *ApJ*, 633, 680
- Berczik, P., Merritt, D., Spurzem, R., Bischof, H.-P., 2006, *ApJ*, 642, L21
- Berentzen I., Preto M., Berczik P., Merritt D., Spurzem R., 2009, *ApJ*, 695, 455
- Casertano S., Hut P., 1985, *ApJ*, 298, 80
- Cornish N.J., Rubbo L.J. 2003, *Phys.Rev.D*, 67, 022001
- Cutler C., 1998, *Phys.Rev.D*, 57, 7089
- Damour T., Gopakumar A., Iyer B.I., 2004, *Phys.Rev.D*, 70, 064028
- Dieball A., Müller H., Grebel E. K., 2002, *A&A*, 391, 547
- Einsel C., Spurzem R., 1999, *MNRAS*, 302, 81
- Fiestas, J., Spurzem, R. and Kim, E., 2006, *MNRAS*, 373, 677
- Fregeau J. M., Larson S. L., Miller M. C., O'Shaughnessy R., Rasio F. A., 2006, *ApJ Lett.*, 646, L135
- Freitag M., Gürkan M. A., Rasio F. A., 2006, *MNRAS*, 368, 141
- Freitag, M., Rasio, F. A., & Baumgardt, H. 2006c, *MNRAS*, 368, 121
- Gallagher S. C., Charlton J. C., Hunsberger S. D., Zaritsky D., Whitmore B. C., 2001, *AJ*, 122, 163
- Gebhardt K., Pryor C., O'Connell R. D., Williams T. B., Hesser J. E., 2000, *AJ*, 119, 1268
- Gürkan M. A., Freitag M., Rasio F. A., 2004, *ApJ*, 604, 632
- Gürkan M. A., Fregeau J. M., Rasio F. A., 2006, *ApJ Lett.*, 640, L39
- Haehnelt, M. G., Rees, M. J., 1993, *MNRAS*, 263, 168
- Hemsendorf M., 2000, *Dynamics of black holes in galactic centres* (Shaker, Aachen)
- Hemsendorf M., Sigurdson S., Spurzem R., 2002, *ApJ*, 581, 1256
- Hinder I., Herrmann F., Laguna P., Shoemaker D., arXiv:0806.1037
- Komossa S., Burwitz V., Hasinger G., Predehl P., Kaastra J.S., Ikebe, Y., 2003, *ApJ*, 582, L15
- Kustaanheimo P., Stiefel E., *Journal für die reine und angewandte Mathematik* 1965, 218, 204
- Lagoute C., Longaretti P.-Y., 1996, *A&A*, 308, 441
- Longaretti P.-Y., Lagoute C., 1996, *A&A*, 308, 453
- Makino J., Fukushige T., Okumura S.K., Ebisuzaki T., 1993, *PASJ* 45, 303
- Merritt D., 2001, *ApJ*, 565, 245
- Merritt D., Ekers R.D., 2002, *Science*, 297, 1310
- Merritt D., Milosavljević, M., 2004, *ArXiv Astrophysics e-prints*, arXiv:astro-ph/0410364
- Meylan G., Mayor M., 1986, *A&A*, 166, 122
- Merritt, D., Mikkola, S., Szell, A., submitted to *ApJ* (ArXiv:astro-ph/0705.2745)
- Miller M. C., Colbert E. J. M., 2004, *International Journal of Modern Physics D*, 13, 1
- Milosavljević M., Merritt D., 2001, *ApJ*, 563, 34
- Nelemans G., Yungelson L.R., Portegies Zwart S.F., 2004, *MNRAS*, 349, 181
- Peters P.C., 1964, *Phys.Rev.*, 136, B1224
- Porter E.K., Cornish N.J., 2008, *Phys.Rev.D*, 78, 064005
- Portegies Zwart S. F., McMillan S. L. W., 2000, *ApJ Lett.*, 528, L17
- Portegies Zwart S. F., Baumgardt H., Hut P., Makino J., McMillan S. L. W., 2004, *Nat*, 428, 724
- Quinlan G. D., 1996, *New Astronomy*, 1, 255
- Reijns R. A., Seitzer P., Arnold R., Freeman K. C., Ingerson T., van den Bosch R. C. E., van de Ven G., de Zeeuw P. T., 2006, *A&A*, 445, 503
- Rubbo L.J., Cornish N.J., Poujade O., 2004, *Phys.Rev.D*, 69, 082003
- Sesana, A., Haardt, F., Madau, P., 2007, *ApJ*, 660, 546
- Shapiro Key J., Cornish N.J., 2009, *Phys.Rev.D*, 79, 043019
- Shapley H., 1930, *Flights from chaos; a survey of material systems from atoms to galaxies*, adapted from lectures at the College of the city of New York, Class of 1872 foundation., Shapley H., ed.
- Spurzem R., 1999, *Journal of Computational and Applied Mathematics*, 109, 407
- Staneva A., Spassova N., Golev V., 1996, *A&AS*, 116, 447
- Timpano S., Rubbo L.J., Cornish N.J., 2006, *Phys.Rev.D*, 73, 122001
- Thorne, K.S., Braginskii, V.B., 1976, *ApJ*, 204, L1
- White R. E., Shawl S. J., 1987, *ApJ*, 317, 246
- Whitmore B. C., Zhang Q., Leatherer C., Fall S. M., Schweizer F., Miller B. W., 1999, *astj*, 118, 1551
- Yu, Q., 2002, *MNRAS*, 331, 935
- Zhang Q., Fall S. M., 1999, *ApJ Lett.*, 527, L81
- Zier C., Biermann P.L., 2002, *A&A*, 396, 91